BUILDING A RAMAN LASER PUMP SOURCE

CAPABLE OF GENERATING FLEXIBLE PULSE DURATIONS

WHILE MAINTAINING HIGH SPATIAL QUALITY

by

Stephen Scott Wagemann

A thesis submitted in partial fulfillment
of the requirements for the degree

of

Masters of Science

in

Physics

MONTANA STATE UNIVERSITY
Bozeman, Montana

April 2009

APPROVAL

of a thesis submitted by

Stephen Scott Wagemann

This thesis has been read by each member of the thesis committee and has been found to be satisfactory regarding content, English usage, format, citations, bibliographic style, and consistency, and is ready for submission to the Division of Graduate Education.

Dr. Randy Babbitt

Approved for the Department of Physics

Dr. Richard Smith

Approved for the Division of Graduate Education

Dr. Carl A. Fox

STATEMENT OF PUPOSE TO USE

In presenting this thesis in partial fulfillment of the requirements for a master's degree at Montana State University, I agree that the Library shall make it available to borrowers under rules of the library.

If I have indicated my intention to copyright this thesis by including a copyright notice page, copying is allowed only for scholarly purposes, consistent with "fair use" as prescribed in the U.S. Copyright Law. Only the copyright holder may grant requests for permission for extended quotation from or reproduction of this thesis in whole or in parts.

Stephen Scott Wagemann

April 2009

ACKNOWLEDGMENT

It is my pleasure to acknowledge my advisor Prof. William Randall Babbitt who has patiently advised and supported me throughout my research. I would also like to acknowledge Dr. Zeb Barber and Dr. Randy Reibel who have not only acted as mentors, but have also been a wealth of knowledge and experience and to whom I owe the success of this project. Christoffer Renner also deserves acknowledgement for the many frustrating hours he spent with me troubleshooting the laser system and whose talents and skills have been a daily asset. I also must acknowledge Dr. Peter Roos who initially had the idea for this project. Finally, I would like to thank Ray Jones and Mark Perkins at Quantel who have been a valuable source of information and spare laser parts.

TABLE OF CONTENTS

TABLE OF CONTENTS – CONTINUED

LIST OF FIGURES

Figure Page

LIST OF FIGURES - CONTINUED

Figure Page

ABSTRACT

A detailed characterization of a Raman pump laser throughout the construction process is reported. Due to specific requirements for the pulsed Raman experiment, there were no commercially available pump lasers capable of meeting our specifications. The pump source must produce high energy pulses of 50mJ to 100mJ with variable duration centered at 200ns. To create this pump source, the pulses are gated from a CW source and then amplified with a high gain Nd:YAG amplification system. High spatial quality is also a necessity as the laser needs to be coupled into a small diameter waveguide functioning as the Raman cell. The laser was found to operate well, producing the required energy with the desired pulse flexibility. However, the amplification process induced spatial distortion that effectively produced a super Gaussian intensity distribution.

CHAPTER 1

INTRODUCTION

Application and Motivation

The U.S. Armed Forces have aggressively pursued laser technology to enhance their defense capabilities against guided missile threats. A strong emphasis of their current technology is focused around the infrared or near infrared wavelengths where high powered lasers are readily available. This frequency range is ideal for combating heat-seeking devices such as anti-aircraft missiles because this is where their detectors are the most sensitive. Efforts have been made to extend this technology into the visible regime where some missile guidance systems operate. In this regime the preexisting infrared countermeasures are not as effective and can easily be filtered. Unfortunately, frequency doubled light from the common high powered sources falls in a narrow region (typically 532nm), which can be easily blocked with a notch filter. It is possible to get outside of this narrow spectral band using a combination of frequency doubling and optical parametric oscillation. However, this process is complex and requires multiple optical stages. Tunable dye lasers can also operate in the desired regime but they are often cumbersome, expensive, and potentially require the use of carcinogenic dyes. An alternative solution is to use high powered Stokes and anti-Stokes shifted light in waveguides via Stimulated Raman Scattering (SRS). The shifted light generated with this method can be outside the potentially filtered region [1]. SRS also provides access to

a multitude of wavelengths, which are varied depending on the gas used in the waveguide making them difficult to defeat.

By providing high energy access to wavelengths that are difficult to reach using traditional methods, SRS can enhance commercial applications such as long-range LIDAR, laser display systems, wavelength sensitive medical applications, and hyperspectral imaging. Some of these applications currently use multistage sum frequency generation, which is relatively complex and sensitive to misalignment. Many of these wavelengths could be reached more directly using SRS, which requires only a single conversion. Additionally, SRS would allow UV absorbing crystals to be replaced with transparent gas when operating in the UV. Ultimately, if SRS could be implemented using fiber technology it would allow the development of relatively robust and compact solutions to obtaining these difficult wavelengths thus fulfilling a multitude of industrial and military needs.

Introduction to Stimulated Raman Scattering

There are several ways photons interact with particles in nature. The probabilities of these interactions are strongly dependant on the relative size of the interacting particle and the wavelength of the photon. If the photon's wavelength is roughly the same as the diameter of the particle then Rayleigh scattering will most likely ensue. In this case the scattered photon will have the same frequency as the incident photon. This however, does not always occur. If the particle is a molecule that can be vibrationally or

rotationally excited, then there is a small chance that the photon's energy will be shifted via Raman scattering.

The energy shift in Raman scattering stems from the excitation of the vibrational and rotational modes of the interacting molecule. The energy exchange with the molecule is then subtracted from the incident photon. This process is a good example of energy conservation and is generally referred to as the Stokes shift (see Figure 1). A less likely phenomenon is the reversal of this process, which is referred to as the anti-Stokes shift. The fundamental difference lies in the requirement of an excited molecule to impart energy to the photon for the anti-Stokes shift to occur. Thermodynamics tells us that systems are more likely to be found in the ground state at room temp, which is why the Stokes shift is much more likely. The following diagram portrays the changes in energy between the particle and the photon for various scattering processes.

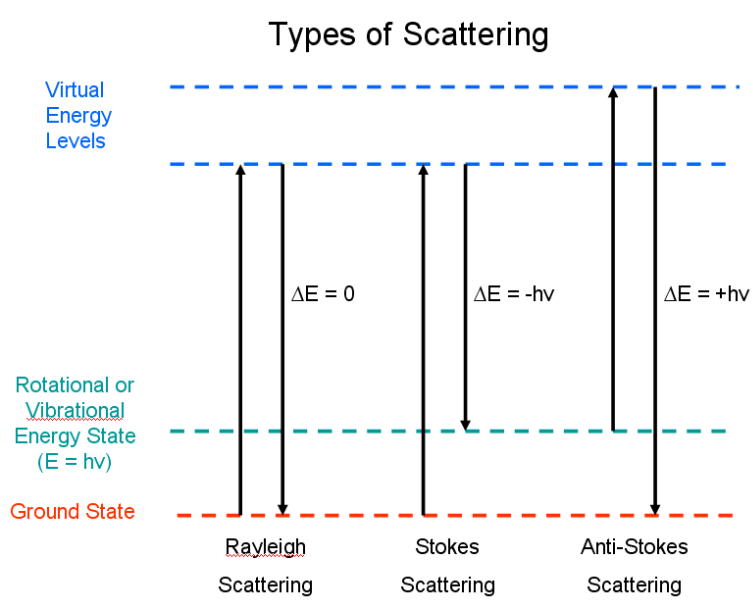

Figure 1.1: Change in photon energy for different types of scattering.

Due to the inherently low probability of Raman scattering, different techniques have been implemented to obtain high conversion efficiencies. One promising method uses laser light coupled into gas filled waveguides, which confine light to a small area over long interaction lengths. The gain for the Raman process is proportional to the intensity of incident light making waveguides ideally suited for SRS. Waveguides have already demonstrated great potential by reducing the threshold for Stokes shifted light from that obtained with high-finesse cavities [2,3]. The general focus of these studies has been Stokes conversion at very low energies leaving the high energy regime and anti-Stokes conversion completely unexplored in hollow-core photonic crystal fibers (HC-PCF).

High intensity light in the proper gain medium is basically all that is required for generating Stokes conversion. However, producing anti-Stokes is a more complicated process. It involves phase matching two pump photons with a Stokes and anti-Stokes photon through a process known as Raman-resonant four-wave mixing (FWM). Unfortunately, unless compensated for, the normal dispersion in Raman gases prohibit phase matching from occurring. A potential advantage to using waveguides over cavities for SRS is that they induce anomalous dispersion in the coupled light. It is therefore theoretically possible to achieve phase matching by adjusting the normal dispersion by pressure tuning the Raman gas [4,5].

In order to generate high energy conversion to Stokes or anti-Stokes in waveguides, a high powered pump laser with exceptional spatial quality is required [6]. The spatial quality is the key to reducing optical damage at the input facet of the

waveguides, which range in size from 5-200 microns. The commercially available lasers that offer the desired energy and spatial quality lack the ability to produce long and flexible pulses because most utilize a single electro-optic Q-switch. The temporal specification on the pump laser is a requirement for the Raman study and also for other applications such as missile defense.

Promising SRS results have recently come from the University of Bath using frequency doubled Nd:YAG as well as a variety of other wavelengths coupled into HC-PCF. Their research has focused primarily on highly efficient Stokes conversion at the lowest possible energies using pulsed and CW pump sources. They have achieved Stokes conversion efficiencies as high as 92% and have seen SRS at lower thresholds than were previously achieved with high-finesse Fabry-Perot cavities [7]. The research carried out at the University of Bath has exclusively used HC-PCF for Stokes conversion and has not yet reported work on high energy conversion.

Though HC-PCFs are a relatively recent discovery, the use of waveguides to generate Raman scattering has been well documented. SRS was first observed in capillaries by Rabinowitz in 1976 where 10 mJ were converted with 46% efficiency. Since this initial experiment, SRS has been studied in capillaries with a variety of gases and pump wavelengths. High energy Stokes conversion has also been seen with pump energies as high as 100mJ over 30ns. Ten years after Rabinowitz's experiment, Hanna generated second and third Stokes shifts in capillaries with 9% conversion efficiency to the third Stokes [8]. Different designs have been implemented including the use of a wave guide in conjunction with a cavity to stretch the limits of the SRS threshold [9].

Small amounts of anti-Stokes have been seen in both high-finesse cavities and waveguides but highly efficient anti-Stokes has not been witnessed until recently by Zaitsu in 2008. He used intracavity dispersion in a high-finesse cavity to compensate for the normal gas dispersion [10]. Highly efficient anti-Stokes conversion has not yet been achieved in waveguides.

Objective

The objective is to build a high powered laser pump source capable of producing efficient high power Stokes and anti-Stokes using hollow core waveguides. The laser must also produce long and flexible pulse durations ranging from 10ns to 300ns with good spatial quality. The pulse flexibility specification is a requirement for laser countermeasures. The desired final output energy is 50mJ of 574nm, which is the first Stokes shift for CO_2 gas. To obtain this goal the pump laser must be capable of producing two to three hundred millijoules of 1064nm. With roughly 30% conversion to 532nm there will be at least 50mJ for SRS. One would assume that with the many commercially available lasers it would be possible to purchase a pump source capable of meeting the temporal, spatial and energy requirements. Unfortunately, the commercial products which meet our energy and beam quality demands lack the desired pulse duration flexibility. For example, the Brilliant laser manufactured by Quantel can produce several hundred millijoules of 532 nm with excellent spatial quality. However, the pulse duration is limited to 8 ns.

Most high energy solid-state lasers use an electro-optic Q-switch which produces pulse durations of about 10ns. Efforts have been made to increase the Q-switching pulse flexibility, but generally require multiple Q-switches controlled by complex power supplies [11]. Another option is a commercially available fiber laser, which offers a very versatile pulse duration and repetition rate. Unfortunately, these lasers are very expensive and operate only at low power. This would be sufficient as a seed source but additional amplifiers would be needed to meet the energy requirement. Rather than purchasing an expensive flexible seed source, one could be built by gating the output of a CW laser with an acousto-optic modulator (AOM). The carved pulses would then be amplified to the desired energy [12]. This method provides a relatively simple solution to generating high energy pulses with flexible duration.

This thesis presents a detailed characterization of a Raman pump laser designed in the previously described fashion. It will begin with a characterization and modification of the CW source that seeds the system's amplifiers. Then the amplification process will be discussed in detail, including numerical modeling and insight into distortion effects. Then the spatial quality of the beam will be characterized followed by a brief introduction to frequency doubling, which is needed to obtain the desired wavelength for the Raman study. There is also a section on coupling and transmission as well as other optical properties related to HC-PCF and capillaries. This thesis will conclude with a discussion on the success of the laser pump source as well as potential improvements. Current Raman results being obtained with the laser system will also be presented. The Matlab

code and scripts for the various models presented in the thesis are included in the Appendices.

CHAPTER 2

INTRODUCTION TO THE LASER SYSTEM

Since there are no commercially available lasers that meet the specific demands of the project, a pump laser must be designed and built. Furthermore, traditional designs for solid-state lasers, which use electro-optic Q-switching techniques, are not viable in this situation, as they do not offer much in the way of pulse flexibility. Therefore an alternative pulse forming method was adopted for the Raman pump laser [12].

Laser Overview

The laser amplification system is based on amplifying low energy pulses gated from a CW seed source. The laser used as the seed source is a diode-pumped solid-state laser (DPSS). This laser generates 1W at 1064nm with reasonable spatial quality and multiple longitudinal modes. To form the desired pulses the CW light is gated with an acousto-optic modulator (AOM) driven by an arbitrary waveform generator (AWG). This technique of pulse generation is very versatile because the AOM can create nearly any pulse shape that the AWG is capable producing within the AOM's bandwidth. Once the pulse is formed it will be amplified by three separate amplifiers. Each amplifier is double passed with an isolator before each stage to suppress pre-lasing. Once the desired energy has been reached the pulses are frequency doubled to study Raman conversion. Figure 2.1 shows the layout of each component in the laser system, followed by Figure 2.2, which is a picture of the setup.

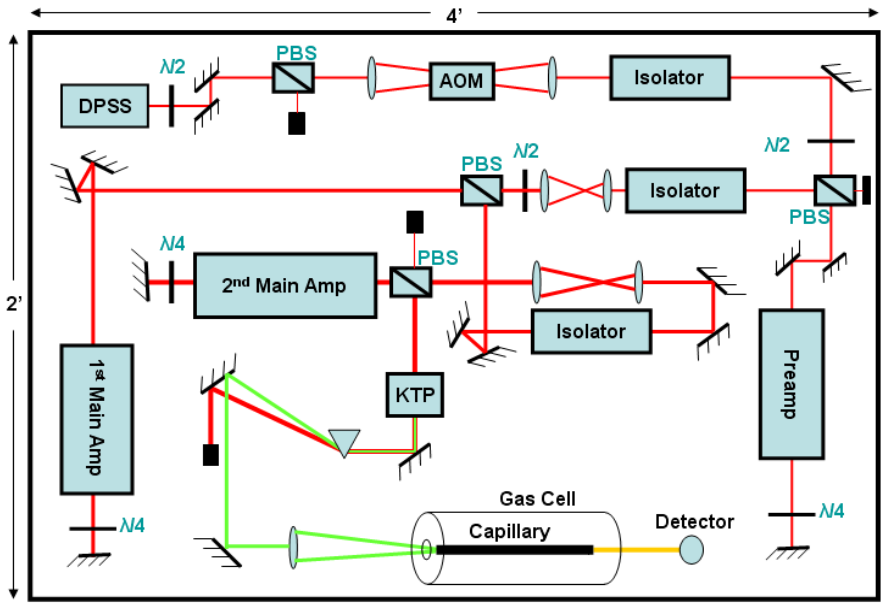

Figure 2.1: The layout of the laser system and all key components. DPSS stands for diode-pumped solid-state laser, AOM refers to the acousto-optic modulator, PBS refers to polarized beam splitter, KTP is the doubling crystal, and $\frac{\lambda}{2}, \frac{\lambda}{4}$ refer to half and quarter wave plates, respectively.

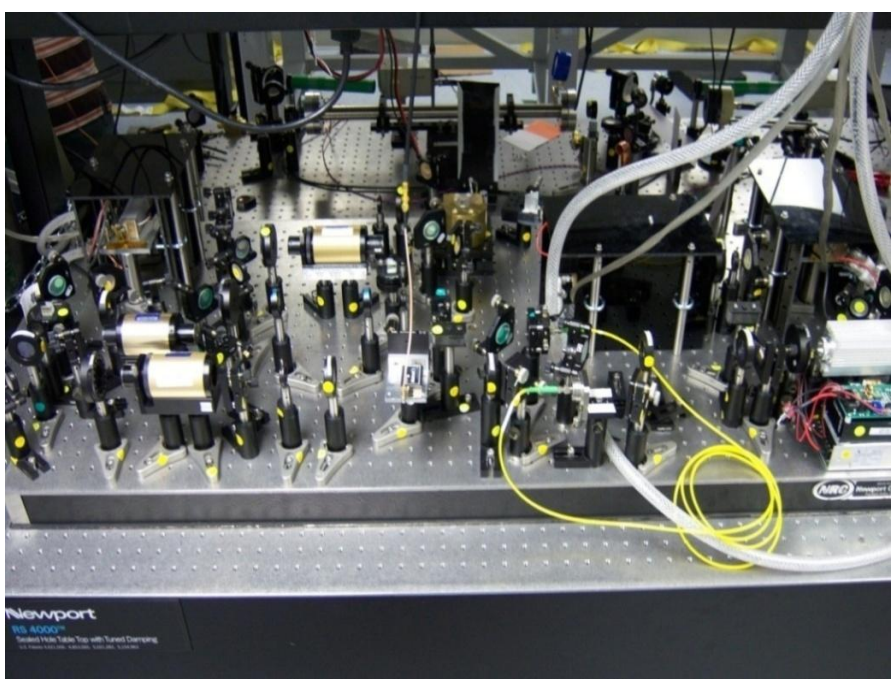

Figure 2.2: Photograph of the laser system with the DPSS in the bottom right hand corner and the Raman cell at the top. The three amplifiers are contained in the black boxes as a safety precaution against their high voltage.

The timing of the amplifiers relative to the input pulse of the DPSS is important for optimizing the energy potential of the system. Ideally the input pulses will enter the amplifiers when their stored energy is maximized. Two power supplies are used to operate the three amplifiers, which were triggered externally. The power supplies have internal delays of 450 and 500 microseconds, which are illustrated in Figure 2.3. The timeline also includes the flash lamp pulses and the fluorescence of the gain mediums for each amplifier, which occur at roughly the same time as per [13].

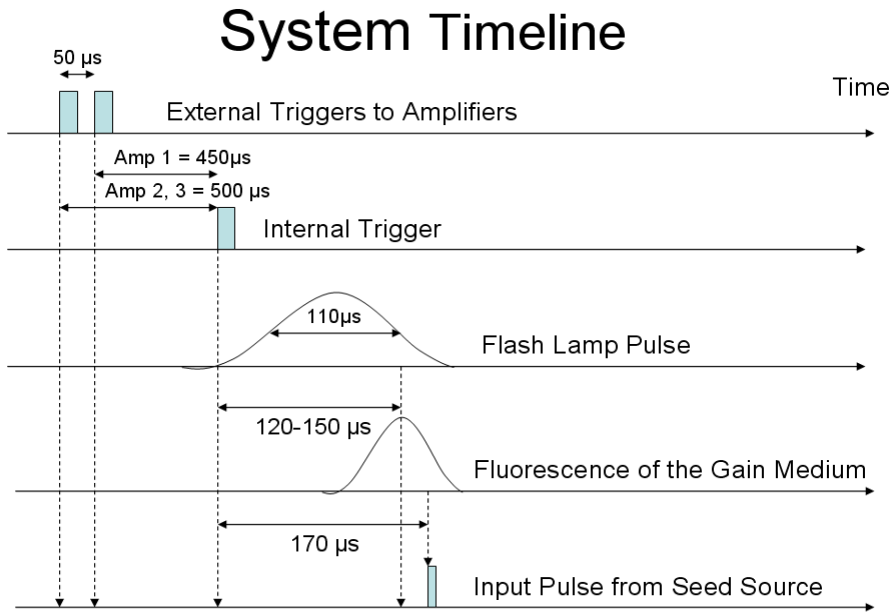

Figure 2.3: System timeline that shows when the amplifiers are triggered relative to the input pulse. The flash lamp pulse duration and gain medium fluorescence are from [13].

Seed Source

The laser system begins with the master oscillator DPSS manufactured in China by Lasever. The DPSS is specified to operate at the TEM_{00} mode with no specification

on the longitudinal modes. The quality of the master oscillator is important because it determines the beam quality and spectral width of the entire system. The gain medium used in the DPSS is Nd:YVO_4, which has more gain than Nd:YAG and roughly the same output wavelength (1064nm). Having the same output wavelength as Nd:YAG is important because the three amplifiers, which will be discussed in the next section, use Nd:YAG as their gain medium. The DPSS was quite inexpensive ($800), which puts its quality into question. To verify that its output wavelength falls within the fluorescence spectrum of Nd:YAG, the DPSS was characterized with an optical spectrum analyzer (OSA). The fluorescence spectrum of Nd:YAG is peaked between 1064nm and 1066nm, which covers the output spectrum of the DPSS as seen in Figure 2.4.

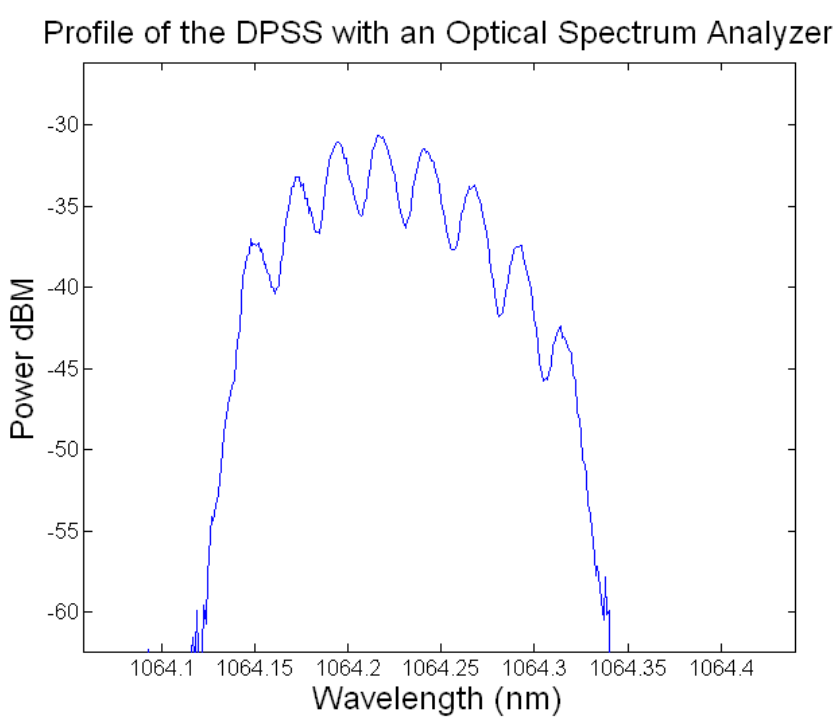

Figure 2.4: The spectrum of the DPSS measured by an optical spectrum analyzer with a resolution of 20pm.

Figure 2.4 was taken at high resolution (20pm) and shows the oscillations in the spectrum of the DPSS. The spacing of the oscillation is the free spectral range, $\Delta\nu$, of the DPSS laser cavity, which is related to the cavity length by Equation 2.1. The spacing was determined from Figure 2.4 to be 5.83GHz, which indicates that the cavity is 26mm long. This length is not specified by the manufacturer and cannot be measured because it is sealed within the laser housing. The length available for the cavity from measuring the exterior of the housing is roughly 40mm, which is consistent the value found above.

$$\Delta\nu = \frac{c}{2nl} \tag{2.1}$$

Generating Variable Pulses

As previously mentioned, the pulses are formed by an AOM controlled by an AWG. This setup allows for arbitrary control of the pulse shape, amplitude, and phase within the constraints of the CW source and the rise time of the AOM. An interesting aspect of the AOM is that there is a tradeoff between the rise time and efficiency, which is governed by the speed of the sound waves traveling through the AOM crystal and the beam focus. The rise time is the time it takes to switch on or off 80% of the diffracted beams as specified by the manufacturer and shown in Figure 2.5.

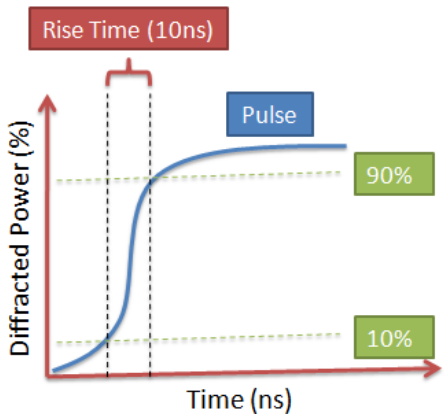

Figure 2.5: Illustrates how the rise time is measured for the AOM.

The AOM works like a variable light switch by using sound waves in a crystal to diffract monochromatic light. The sound waves are generated by a piezoelectric transducer that vibrates when driven by an oscillating voltage. The AOM's optimum driving frequency is 200MHz as specified by the manufacturer and also as determined experimentally by optimizing the diffracted power.

Figure 2.6 shows the AOM's specifications from Crystal Technology's data sheet for model 3200-127. This is the high power AOM used in the laser system. For our application a fast rise time is slightly more of a priority than efficiency. The spot size was chosen to be 25µm, which gives 60% efficiency and a rise time of 10ns.

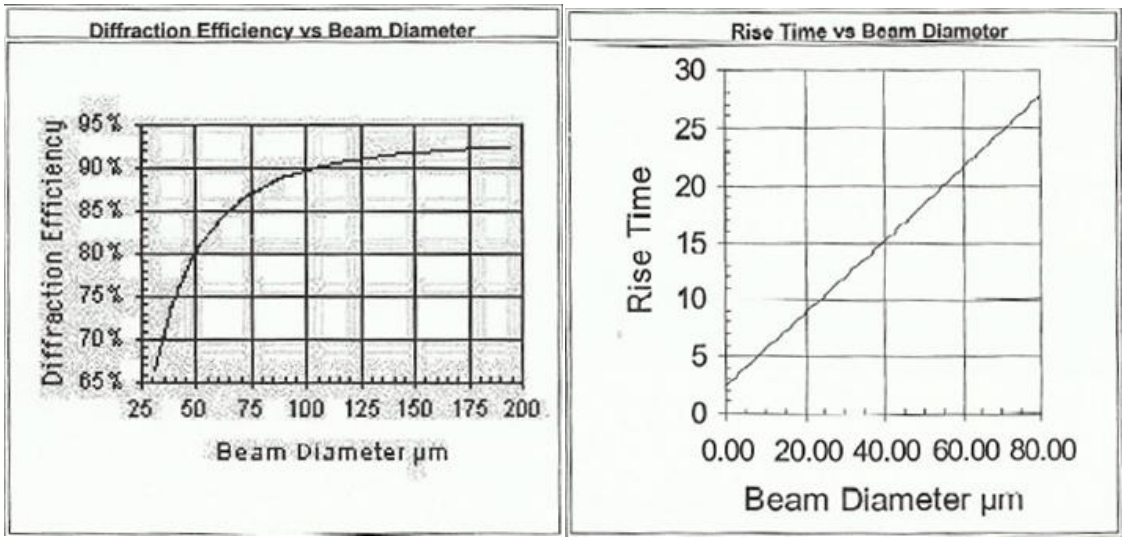

Figure 2.6: Efficiency and rise time (ns) versus beam size of acousto-optic modulator as specified by the manufacturer (Crystal Technology Inc.).

CHAPTER 3

AMPLIFICATION

The amplification process starts by storing energy in a gain medium by creating a population inversion of the ions. Once a majority of the ions are excited, the initial pulse is passed through the excited gain medium, which stimulates the emission of photons. The photons produced via stimulated emission have the same polarization, wavelength, direction, and phase as the stimulating photon thus resulting in an increase in amplitude of the initial pulse. The characteristics of stimulated photons constitute the properties that uniquely define a laser's performance.

The system is designed to produce pulses of varying size and shape. The initial tests used a pulse duration of 200ns, which is long enough to clearly see temporal distortion effects. At this pulse duration, the one watt output of the DPSS produces 80nJ per pulse with 40% transmission through a spatial filter and the AOM combined. In order to increase this pulse energy to the desired 200mJ the amplifier system must increase the power of the input pulse 2.5×10^6 times. This is by no means a trivial undertaking. The biggest obstacle is pre-lasing by way of parasitic oscillation [14]. In other words, any scattered or reflected light in the system will be amplified up to 2.5×10^6 times. This creates the issue of uninvited oscillation throughout the system, which will not only deplete power but will also greatly increase the risk of optical damage. To overcome this, isolation is required for every three orders of magnitude of gain. This is accomplished by splitting the amplification system into three stages while placing

isolation before each stage. Once properly isolated, the laser should be able to operate without the risk of parasitic oscillation. Residual light diffracted by the AOM when it is switched off could also be a source of pre-lasing, however, controlling the AOM with an AWG reduces this risk.

The first amplification stage is the preamplifier, which has a disproportionately high percentage of the system's gain and is consequently at the greatest risk for pre-lasing. The next two stages are the main amplifiers that produce the majority of the energy. The general idea is to have enough gain in the preamplifier to obtain the maximum possible extraction efficiency from the main amplifiers. It may seem counterintuitive that input pulses of less intensity experience more gain, but extract less energy than pulses of higher intensity. This is because high energy pulses substantially deplete the energy stored in the gain medium consequently reducing the amplifier's gain. This concept will be discussed in more detail later in the chapter.

Preamplifier and Small Signal Gain

As can be seen in Figure 2.1, the gated pulses leave the AOM and immediately enter the first stage of amplification. This stage begins with a Faraday isolator, which protects the AOM and the master oscillator from any amplified back reflections. Once properly isolated, the pulses are amplified up to 30 times per pass for a double pass gain of 900 using a gain module from an Ultra laser from Quantel. Double passing is achieved by placing a polarizing beam splitter (PBS) in front of the amplifier and a quarter wave plate followed by a mirror after the amplifier [15]. Double passing the

quarter wave plate induces a half wave phase shift, which effectively changes vertically polarized light to horizontal and vice versa. This allows the PBS to redirect the beam on its second pass. To further reduce the chance of parasitic oscillation, it is a good idea to ensure that the beam's first pass does not spatially overlap with its second pass at the PBS.

The Ultra gain module is capable of producing 50mJ at 1064nm when operating within the Ultra laser. When used as a preamplifier, it will extract a mere fraction of this energy producing only 50μJ. The small energy extraction is attributed to the pulse energy entering the preamplifier, which is very small compared to the energy stored in the amplifier. In this situation an amplifier is considered to be operating in the small signal gain regime. This allows the amplification process to be modeled as though the stored energy is not depleted by the passing pulse. The equation for small signal gain is found by solving the equation for stimulated emission and is given by Equation 3.1.

$$\frac{dI}{dz} = \sigma_{2,1} * \Delta N_{2,1} * I(z) \tag{3.1}$$

In this equation, I is the intensity, $\sigma_{2,1}$ is the scattering cross section and $\Delta N_{2,1}$ is the population inversion density, which is proportional to the amplifier's pump energy. Since the population inversion will remain constant, the first two terms can be combined into a single gain coefficient, γ. This equation is separable so integrating will lead directly to the small signal gain, G_0.

$$\frac{I(z)}{I_{in}} = G_0 = e^{\gamma z} \tag{3.2}$$

The gain coefficient can easily be determined experimentally and like the population inversion, it depends on the amplifier's pump energy. However, if the gain is not given by the manufacturer, calculating it theoretically can prove to be extremely difficult. For example, when purchasing an amplifier that does not have a specified gain, being able to calculate the small signal gain before the purchase is a necessity. A quick and easy method to calculate the small signal gain is to scale the pump energy and cross sectional area of the gain medium with that of a known amplifier. The accuracy of this method was found to be 3% for the amplifiers used in this project but depends on the pump cavity design among other variables. This shortcut is much easier than calculating the lamp efficiency, η_{lamp}, outright, which requires knowing the energy transfer efficiency for several transitions [16]. This relationship is shown in Equation 3.3.

$$\eta_{lamp} = \eta_e \eta_\nu \eta_g \eta_a \eta_s \eta_q \tag{3.3}$$

The lamp efficiency is defined as the ratio of the energy stored in the gain medium to the energy provided by the power supply. It is dependent on the efficiency of the pump light emitted by the flash lamp or diode to the input electrical power, η_e, the overlap of the output spectrum of the flash lamp or diode and the absorption bandwidth of gain medium, η_ν, the ratio of the pump light that enters the gain medium to the total

emitted pump light, η_g, the fractional absorption of the gain medium, η_a, the quantum defect efficiency, η_s, and the quantum efficiency of non-radiative decay from the pump band to the upper lasing level. Rather than going through these calculations, the lamp efficiency was determined experimentally.

The first step in determining the amplifier lamp efficiencies is to characterize the three amplifiers separately with the DPSS. In doing so, it was found that the gain of each amplifier increased exponentially with increasing pump energy and with no temporal pulse distortion. This indicated that each amplifier operated in the small signal gain regime if operated separately. This is expected because the 80nJ pulse energy generated by the DPSS is much less than the hundreds of millijoules stored in each of the amplifiers. The uniform temporal amplification is evident in Figure 3.1 and the exponential gain increase for the three amplifiers is shown in Figures 3.2-3.4.

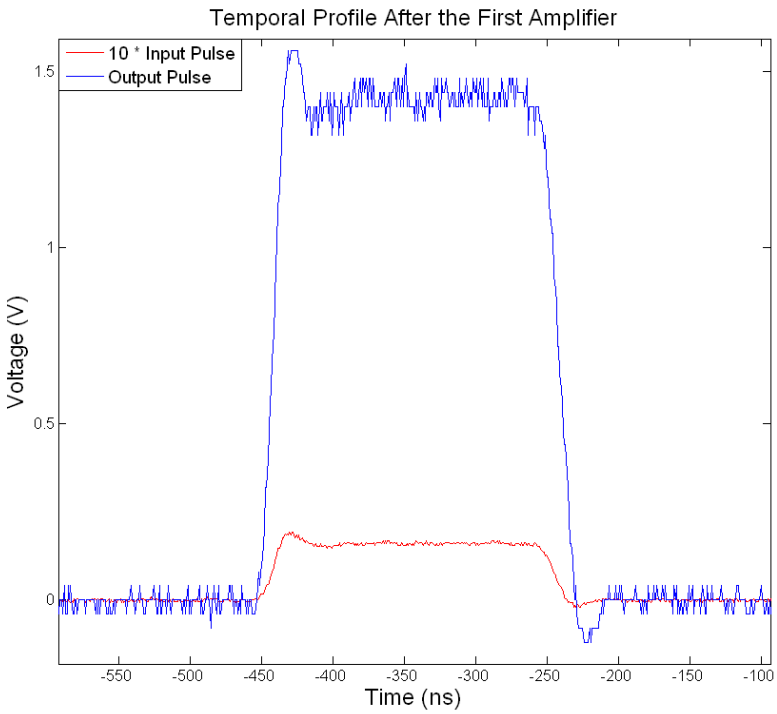

Figure 3.1: Temporal profile before and after amplification by the first amplifier. Similar results were produced with all three amplifiers.

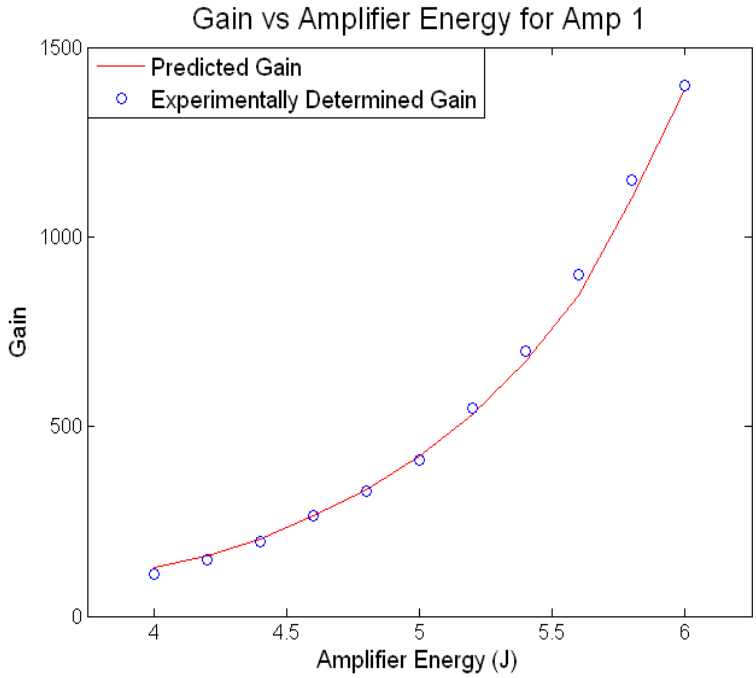

Figure 3.2: Gain versus amplifier energy of the first amplifier operating in the small signal gain regime. The input pulse of 80nJ is generated by the DPSS.

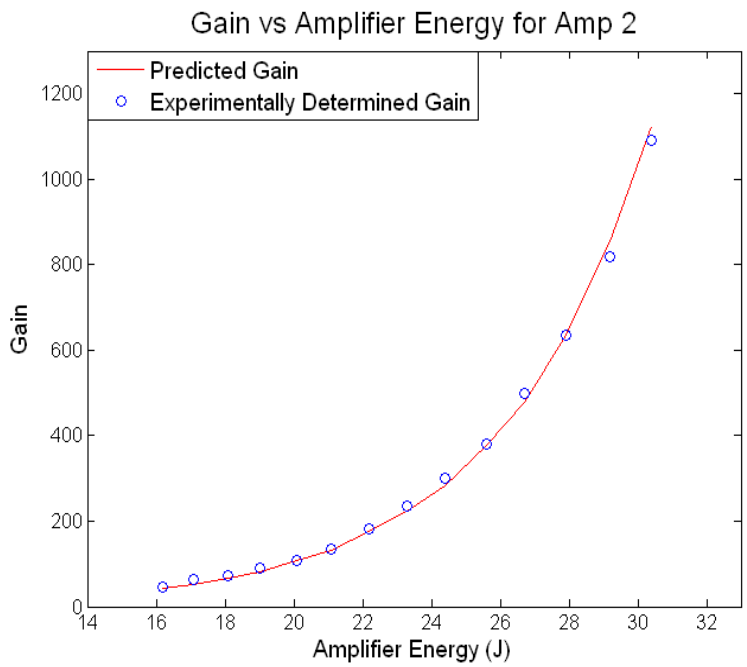

Figure 3.3: Gain versus amplifier energy of the second amplifier operating in the small signal gain regime. The input pulse of 80nJ is generated by the DPSS.

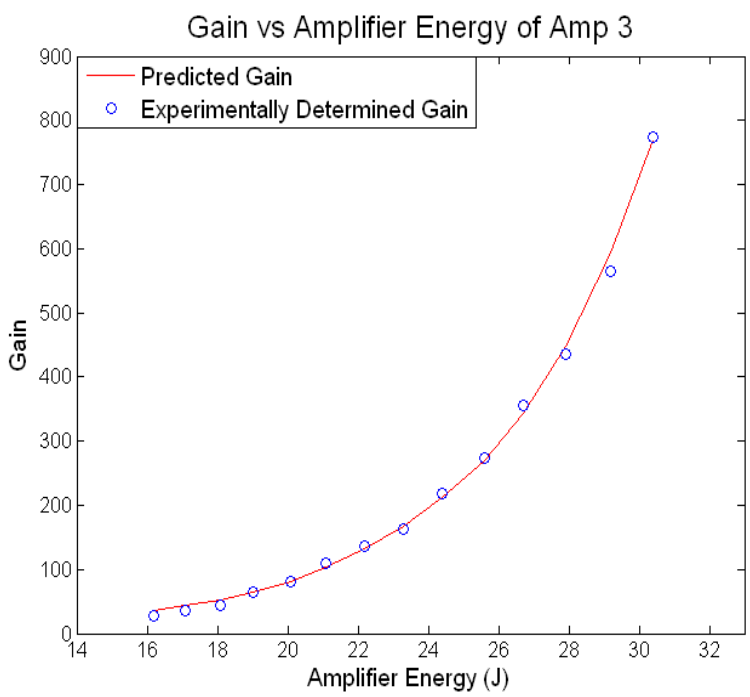

Figure 3.4: Gain versus amplifier energy of the third amplifier operating in the small signal gain regime. The input pulse of 80nJ is generated by the DPSS.

The predicted exponentially increasing gains in figure 3.2-3.4 were scaled using the data points that exhibited the most gain for each amplifier. This scaling factor, η_{lamp}, is the lamp efficiency for each amplifier as shown in equations 3.3 and 3.4. Once the lamp efficiency is known, the population inversion can be calculated as a function of the amplifier's pump energy, E_{pump}. The calculated population inversions were used to generate the predicted gain curves in Figures 3.2-3.4 with Equations 3.1, 3.2. Knowing an amplifier's population inversion is essential for modeling the gain in both the small signal and saturation regimes and are displayed in Figure 3.5. The stored energy, E_{st} is related to the population inversion, ΔN, the volume of the gain medium, V, the ion density, n_{ion}, Plank's constant, h, and the absorbing pump frequency, ν as shown in Equation 3.5.

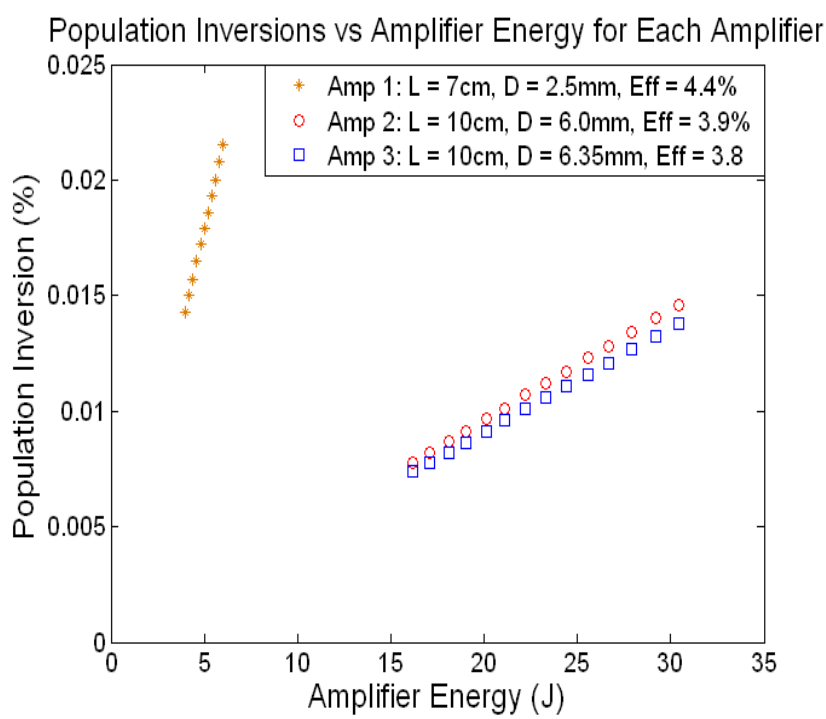

Figure 3.5: Population inversion of each amplifier as a function of amplifier energy. Also includes the length, L, and diameter, D, of each laser rod and the lamp efficiency, Eff, of each amplifier.

$$\eta_{lamp} = \frac{E_{st}}{E_{pump}} \tag{3.4}$$

$$E_{st} = \Delta N * V * h * \nu * n_{ion} \tag{3.5}$$

The experimental efficiency only requires setting the small signal gain (Eqn. 3.1) equal to the experimentally determined gain and solving for the population inversion. From the population inversion the stored energy can be found and then compared to the input energy of the power supply to find the efficiency. The lamp efficiency is 4.4% for the first amplifier, 3.9% for the second amplifier and 3.8% for the third amplifier. Using the lamp efficiencies the predicted gains can be calculated for different input energies of the power supplies. This is the method used to generate the curve that is graphed with the data in Figures 3.2-3.4.

Main Amplifier and Saturation Regime

The two main amplifiers are made from the gain modules of CFR model lasers also manufactured by Quantel. A modified power supply is used that increases their energy capability from 400mJ to well over a Joule per amplifier. The gain of the first amplifier is 25 per pass and the second is 20 per pass. They are both operated by the same power supply but the gain in the second is less than the first due to a larger cross-sectional area of its gain medium. The larger area allows for less fluence, which reduces

the potential for damage at the final amplifier where the energy levels are the greatest [17].

Saturation intensity, I_{sat}, is a useful value when discussing how an input pulse will be amplified. This value serves as a divider between the small signal and saturation amplification regimes in an amplifier. If the input pulse intensity is much less than the saturation intensity then the population inversion will not be substantially depleted and the amplifier will effectively remain in the small signal gain regime. However, as the input pulse intensity surpasses the saturation intensity, the gain medium is substantially depleted and the amplifier enters the saturation regime. The saturation intensity also determines the point where spontaneous emission and stimulated emission are equal. The saturation intensity contains several important constants including the stimulated emission cross section, $\sigma_{2,1}$, the lifetime of the upper lasing state, τ_2, Plank's constant, h and ν is the laser's operating frequency [18].

$$I_{sat} = \frac{h\nu}{\sigma_{21}\tau_2} \tag{3.6}$$

The primary consequence of entering the saturation regime is that the initial pulse is no longer uniformly amplified. This is due to the dependence of the gain on the population inversion, which is depleted as the pulse evolves. The gain, G, depends exponentially on the frequency dependant stimulated emission cross section, $\sigma_{2,1}$, the

population inversion density, $\Delta N_{2,1}$ and the length traveled through the gain medium, 2L. This relationship is give by Equation 3.7.

$$G = e^{\int_0^{2L} \Delta N_{21}(z) * \sigma_{21} * dz} \tag{3.7}$$

As photons are stimulated, excited electrons are driven to the lower lasing level causing a reduction in the population inversion and consequently the gain. This happens simultaneously with the amplification which causes the front of the pulse to experience more gain than the rear of pulse. The longer the pulse, the more it is distorted, which unfortunately means that the relatively long 200ns pulses generated by this laser system will be severely distorted.

Modeling and Compensating for Temporal Pulse Distortion

In order to prevent pulse distortion and to produce the desired pulse shape, the input pulse can be appropriately pre-shaped to combat the amplification distortion. The correct pre-shape can be approximated using the gain equation but only if an amplifier's population inversion is known through all space and time. Since all the energy states are coupled, it is necessary to model the population of every state involved in the lasing process to track the population inversion. This can be accomplished by numerically solving the system of coupled rate equations governing the energy states.

Nd:YAG is a four level lasing medium, as shown in Figure 3.6, which means there are four energy states involved in the lasing process. The upper most energy state is

actually a compilation of states and is often referred to as a pump band. The transition from the pump band to the upper lasing level occurs very rapidly compared to the lifetime of the upper lasing level. It is therefore a safe approximation to consider the population of the pump band negligible. The upper lasing level is a metastable state with a relatively long life time of 230 microseconds. Unlike the upper lasing level, the lower lasing level decays very rapidly to the ground state. The fast transition of the lower lasing level is the key element that causes four level lasers to be twice as efficient as three level lasers [19].

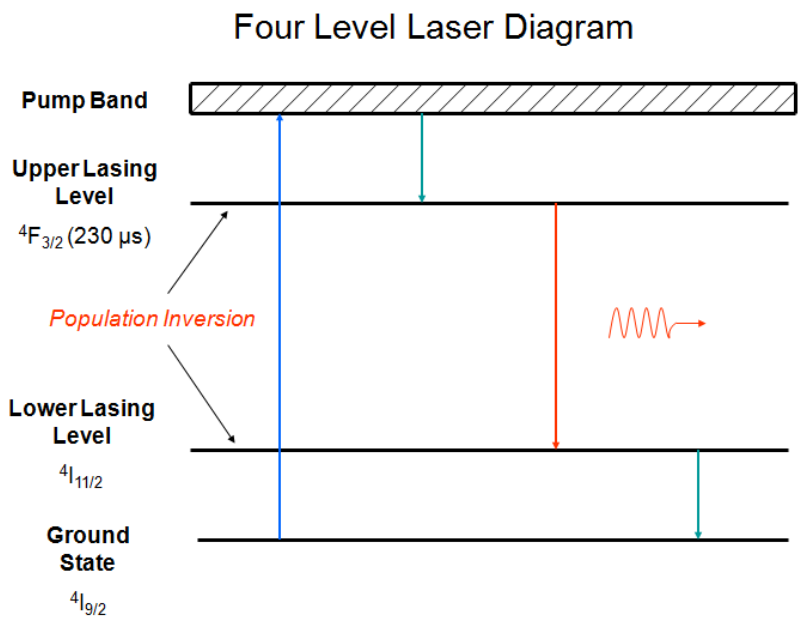

Figure 3.6: Diagram of the four level lasing system of Nd:YAG, which is the gain medium used in the three system amplifiers.

Ions will populate and depopulate the three remaining energy states via stimulated emission, spontaneous emission, and absorption. Taking these processes into account it

is possible to model their populations using three coupled differential equations (one for each state). The following equations are generally referred to as the laser rate equations for the fractional populations, $N_{0\text{-}2}$, where 0, 1 and 2 stand for the ground state, lower lasing level, and upper lasing level, respectively.

$$\frac{dN_2}{dt} = R_2 - \frac{N_2}{\tau_2} - \frac{I_{in}}{\tau_2 I_{sat}}(N_2 - N_1) \tag{3.8}$$

$$\frac{dN_1}{dt} = R_1 + \frac{N_2}{\tau_{21}} - \frac{N_1}{\tau_{10}} + \frac{I_{in}}{\tau_2 I_{sat}}(N_2 - N_1) \tag{3.9}$$

$$\frac{dN_0}{dt} = \frac{N_1}{\tau_{10}} + \frac{N_2}{\tau_{21}} - R_1 - R_2 \tag{3.10}$$

Before moving on to the theoretical model (see Appendix A for modeling script), it is important to understand how each term in the above equations contributes to the flow of ions. Looking at Equation 3.8, the first term on the right hand side is the relatively slow pumping rate R_2. The pulses are much shorter than the pumping rate, which allows R_1 (and R_2) to be neglected. The second term describes the spontaneous emission from the upper lasing level and the last term describes the stimulated emission from the upper to the lower lasing levels. In Equation 3.9 the second and third terms describe the spontaneous emission from the upper lasing level to the lower lasing level and lower lasing level to the ground state respectively. The fourth term shows the increase in excited electrons produced in the lower lasing level from stimulated emission from the upper lasing level. Equation 3.10 describes the increase in ions in the ground state from

spontaneous emission of the lasing states with the first two equations and the third and fourth terms are the pumping rates.

These equations are solved numerically using the fourth order Runge Kutta method (RK4) [20]. They are first integrated over time for the duration of the pulse and then in position over the length of the gain medium. However, since the pulses are 200ft long and each amplifier is only 10cm long, double passing will cause the pulses to overlap on themselves. It is extremely difficult to correlate the timing of the return of the front end with the initial pass of the rear portion of the pulse. Rather than experimentally calculating this correlation, the model's time integration has each time segment double pass an amplifier before the proceeding segment starts its first pass. In other words, the pulse is divided up into segments that are each integrated over the length of the laser medium sequentially. If the time segments of the pulse are chosen to be small enough then this assumption should not significantly impact the predicted population inversion. This process is done in series for all three amplifiers. The model also assumes a constant spatial intensity distribution, which could have an adverse affect on the model's gain prediction.

The first real test of the model was to predict the gain of the entire laser system using the population inversions calculated for each amplifier from the small signal gain. The full system operates in the saturation regime where the gain does not increase exponentially with increasing amplifier energy and where there is substantial pulse distortion. In Figure 3.7 the model predicted the experimental results with reasonable

accuracy; however, the prediction could be improved by not assuming that the beam has a constant spatial intensity distribution.

Figure 3.7 indicates that the desired system gain of 2.5×10^6 has been achieved. The gain is measured by comparing the system output of the unamplified pulse (80mJ) versus the amplified pulse and therefore does not take into account losses in the system, which are 70% for an unamplified pulse. The data point corresponding to a gain of 13.8×10^6 in Figure 3.6 produced 200mJ per pulse. This is a gain of 2.5×10^6 when the system losses are taken into account. The amplifier energy mentioned in Figure 3.7 is the energy stored in the power supply's capacitor that powers the amplifier's flash lamp.

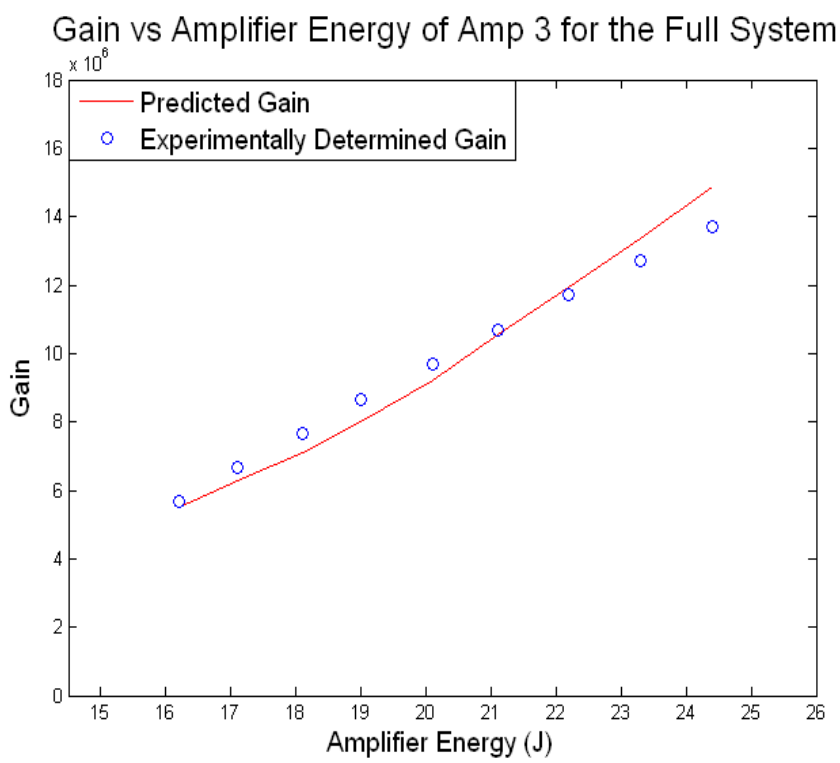

Figure 3.7: Gain of the entire system starting with an 80nJ pulse versus the amplifier energy of the third amplifier operating in the saturation regime.

The model can also predict amplified temporal distortion because it keeps track of the population inversion throughout the duration of a pulse. The model also indicates that it is possible to compensate for the distortion by pre-shaping the input pulse. Figures 3.8-11 show the distortion of different input pulses superimposed on the prediction output by the model. In Figures 3.8-11 the input pulses were captured with a photodiode and an oscilloscope. The input pulses were then amplified with the model to predict the amplified temporal shape. An unfortunate side effect is the numerical amplification of artifacts associated with the detector's background noise, which is substantial towards the beginning of the pulse. Overall, the model predicted the distortion extremely well.

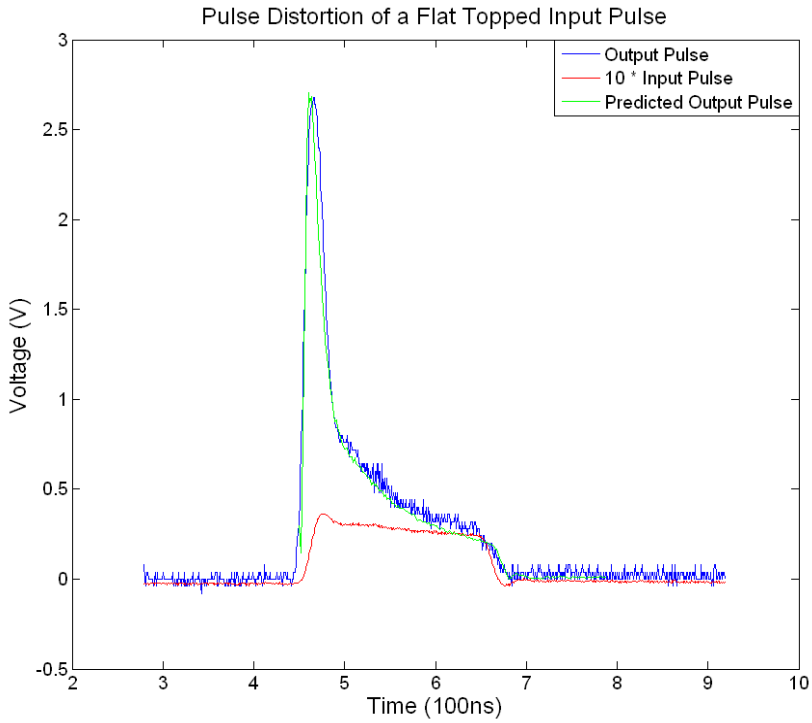

Figure 3.8: Model's predicted pulse distortion of a temporally flat input pulse plotted with the actual input and output pulses.

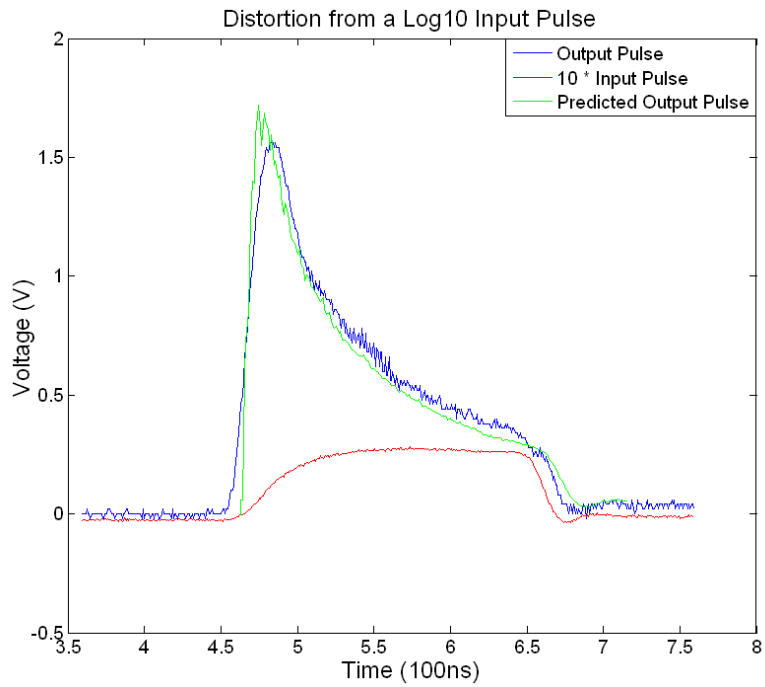

Figure 3.9: Model's predicted pulse distortion of a $\log_{10}$ input pulse plotted with the actual input and output pulses.

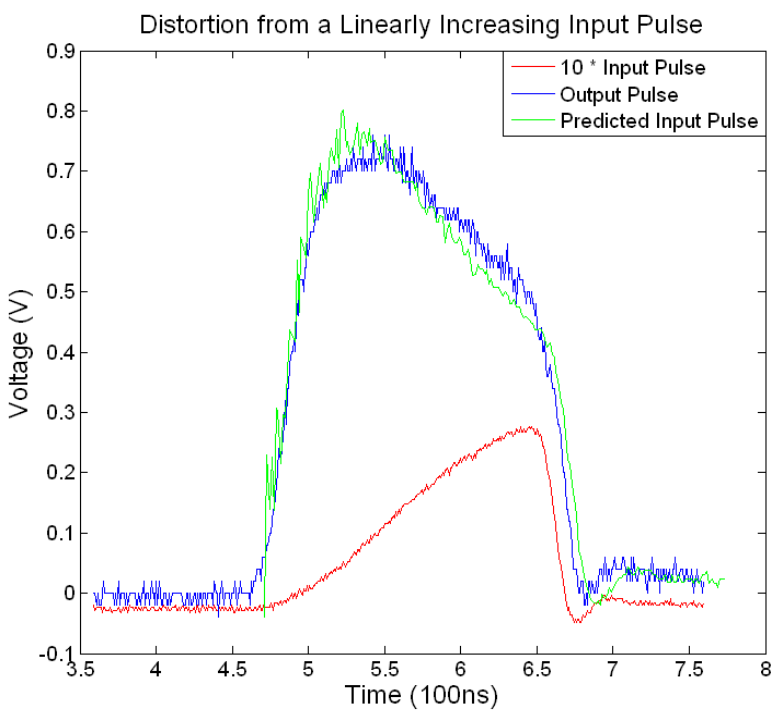

Figure 3.10: Model's predicted pulse distortion of a linearly increasing input pulse plotted with the actual input and output pulses.

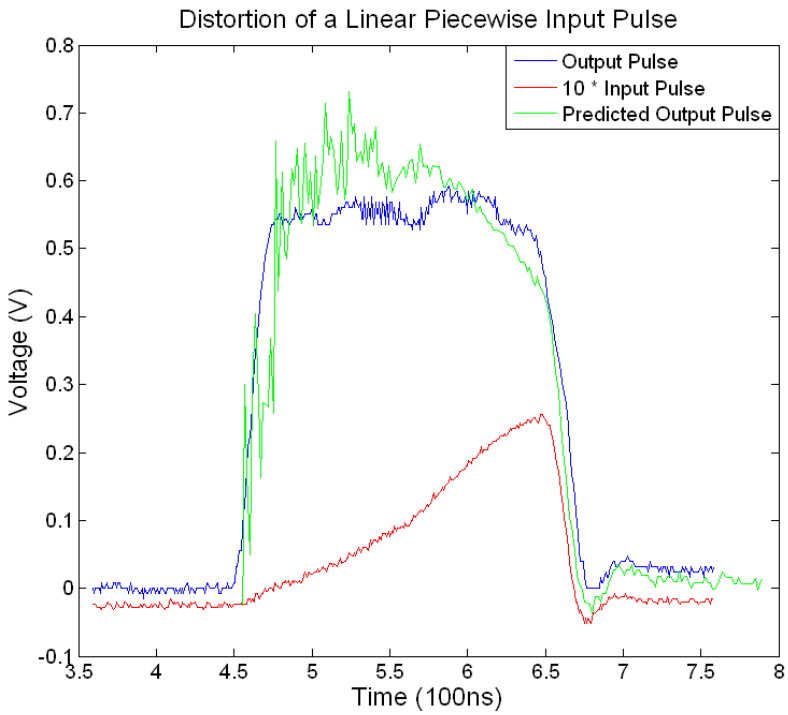

Figure 3.11: Model's predicted pulse distortion of a three segment piecewise linear input pulse plotted with the actual input and output pulses. This pre-shape produced the most temporally flat output pulse.

The input parameters required for the model include the initial population inversion, the input pulse intensity, the length of the input pulse, and also the scattering cross section and lifetimes of the lasing levels. These predetermined values were used to predict the pulse distortions. A scaling factor was used to match the amplitudes of the predicted and experimentally determined amplified pulses. Figures 3.8-11 show the amplification of a temporally flat pulse, a $A*\log_{10}(t+a)$ pulse, a linearly increasing pulse, and a three segmented piecewise linearly increasing pulse, respectively. These test shapes were used, among others, to find which pre-shape best nullified the amplification distortion. The piecewise linear pulse produced the most temporally flat pulse, which varies in amplitude by only 5%.

CHAPTER 4

SPATIAL CHARACTERIZATION

Since the laser is designed to be coupled into a waveguide, producing an output beam of good spatial quality is imperative. For most waveguides a Gaussian beam will optimize the coupling efficiency, thus reducing the potential for optical damage at the input facet of the waveguide. Any part of the beam that is not coupled will be incident on the input facet of the waveguide. Even small amounts of discarded energy can result in very high intensity into the bulk material surrounding the waveguide because very tight focusing is required to couple into small diameter waveguides. The high intensity light is likely to induce optical damage in the bulk material [21]. Coupling with a Gaussian beam further reduces the risk of damage by preventing spatial mode interference resulting in high intensity "hot spots" in the beam.

Laser beam quality is often characterized by the beam parameter product (BPP). It is also referred to as the M^2 parameter, which for a perfect Gaussian beam is equal to one. The BPP is derived from the increased divergence, θ, and spot size, ω, of a beam that contains a superposition of the TEM_{00} and higher order modes. The spot size is defined by the half width of the 1/e point of a Gaussian beam. The divergence of all higher order modes can be described by a scalar quantity times the divergence of a TEM_{00} mode, which is diffraction limited. The properties of imperfect beams can be approximated by substituting their divergence and spot size in terms of the Gaussian

values, θ_0 and ω_0 times the scalar M into equations governing Gaussian beam propagation (Equations 4.1 and 4.2).

$$\theta = M\theta_0 \tag{4.1}$$

$$\omega = M\omega_0 \tag{4.2}$$

Due to the inherent importance of the beam quality an accurate technique for calculating the BPP is imperative. The most commonly used method is to image the beam width at different locations through a focus; this technique is illustrated in Figure 4.1. The measurements can be taken by placing a CCD at different locations through the focus. The CCD records the intensity distribution of the beam, which can then be fit with the Gaussian function given by Equation 4.3, to find the beam width, ω (see Appendix B for modeling script). Equation 4.3 shows the one dimensional intensity distribution of a Gaussian beam, I, in terms of the intensity amplitude, I_0 and the beam width.

$$\mathrm{I} = \mathrm{I}_0 \mathrm{e}^{-\frac{2\mathrm{x}^2}{\omega^2}} \tag{4.3}$$

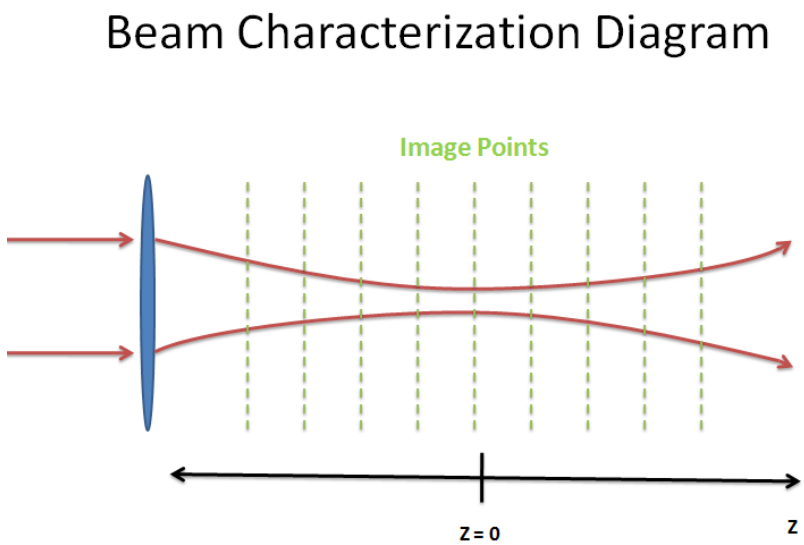

Figure 4.1: Illustrates how the beam width was measured with a CCD in order to determine the spatial quality of the beam.

Once the beam width is known at several locations, the data is fit with the equation describing the beam width of a focusing Gaussian beam along the direction of propagation. The smallest value of the beam width is called the beam waist, ω_0, which is located at the position, z_0. In the fitting program, the parameters are ω_0, M^2, and z_0 are optimized using standard MATLAB fitting routings (see Appendix C for modeling script).

$$\omega = \omega_0 \sqrt{1 + M^4 (\frac{z}{z_r})^2} \tag{4.4}$$

The Rayleigh range, z_r, is in terms of the wavelength, λ and the beam waist. This relationship is shown in Equation 4.5.

$$z_r = \frac{\pi {\omega_0}^2}{\lambda} \tag{4.5}$$

Characterization of the Seed Source

To test the measurement technique, a 532nm Coherent Verdi laser was used. Although this laser has good spatial quality, to ensure a near perfect mode, the Verdi was first coupled into a single mode fiber before imaging. If the beam characterization technique worked correctly, the calculated M^2 value should be very close to one. This is assuming of course that no aberrations are introduced between the fiber and the CCD. The measured M^2 value is 1.06 for the Verdi coupled into the SMF, which indicates that the error of the beam characterization method is within about 7%. Figures 4.2 and 4.3 show the characterization of the Verdi and the DPSS respectively.

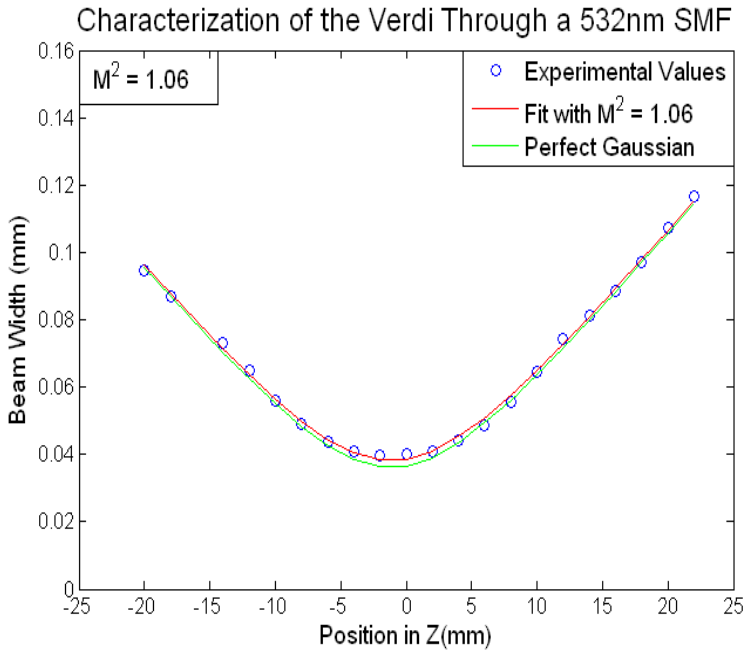

Figure 4.2: Beam size of the Verdi laser after being spatially filtered by a 532nm SMF and then focused by a 200mm plano-convex lens. This data is fit to Equation 4.4 and plotted with a perfect Gaussian beam of the same initial beam width for reference.

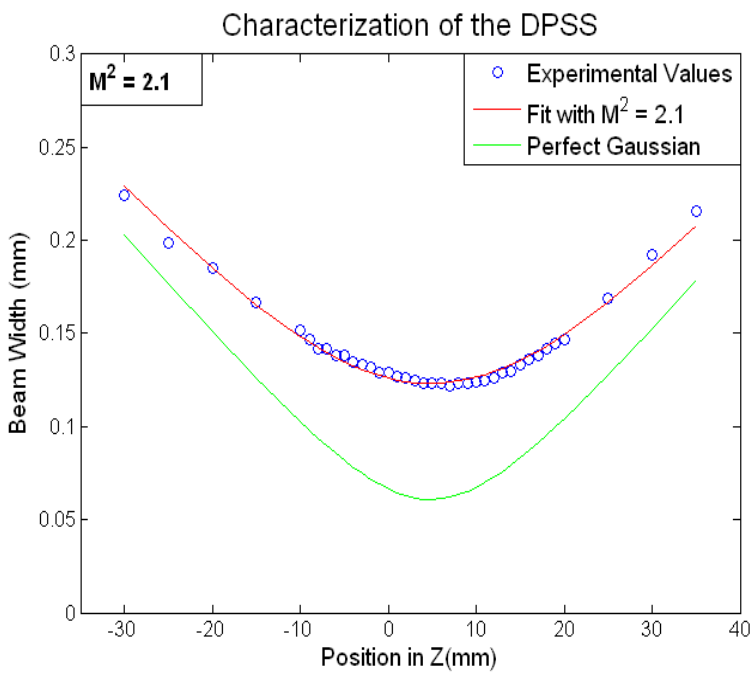

Figure 4.3: Beam size of the DPSS laser focused by a 200mm plano-convex lens and then fit to Equation 4.4. A perfect Gaussian beam of the same initial width is also plotted for reference.

The BPP for the DPSS laser was found to be over two, which is much higher than the 1.1 specified by the manufacturer. Coupling into the waveguides with a BPP of this magnitude will lower the efficiency by up to 75%. Fortunately, the spatial quality can be improved by spatially filtering the beam with a SMF as was done with Verdi. Initially only a 1550nm SMF was available, which might suffice if wrapped into a tight coil. Wrapping the SMF increases the loss in the higher order modes. The output of the 1550nm fiber was then characterized using the same technique as was used for the Verdi. The output of the 1550nm SMF has a BPP of 1.04, which is a considerable improvement over the unfiltered DPSS as seen in Figure 4.4. Unfortunately, wrapping the fiber reduced the transmission efficiency to 40%, which would reduce the potential output energy of the laser system.

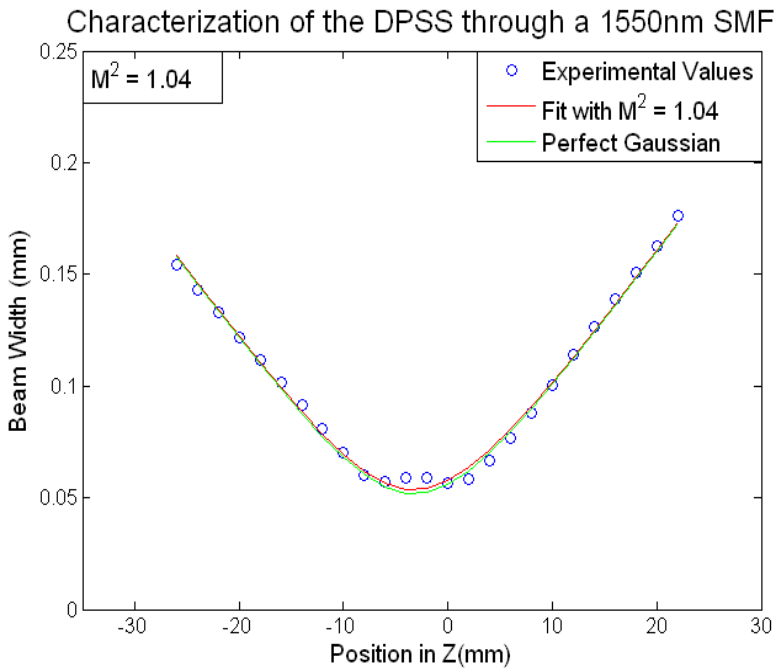

Figure 4.4: Beam size of the DPSS laser focused by a 200mm plano-convex lens after being spatially filtered by a 1550nm SMF. This data is fit to equation 4.4 and plotted with a perfect Gaussian beam of the same initial beam width for reference.

Interestingly there was a small increase in spot size at the beam waist, which can be seen in Figure 4.4. The characterization was repeated several times to ensure that beam size fluctuation was not induced by aberrations imparted to the beam from the characterization process. This unusual characteristic was seen each time the beam was characterized, which indicates that it is part of the propagating mode in the 1550nm SMF and that a 1064nm fiber would be required. The 1064nm SMF eliminated this beam size fluctuation as seen in Figure 4.5.

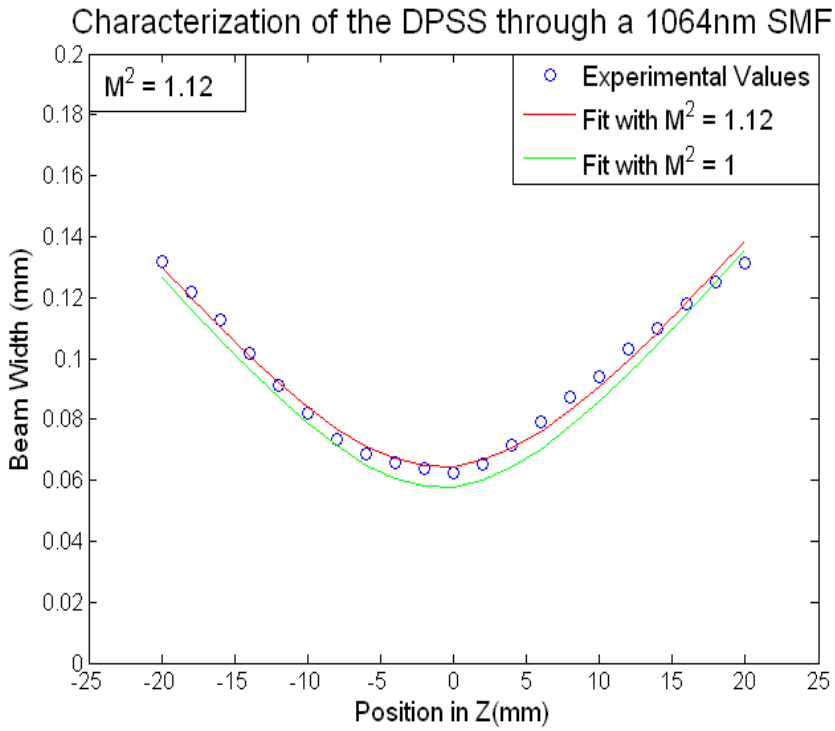

Figure 4.5: Beam size of the DPSS laser focused by a 200mm plano-convex lens after being spatially filtered by a 1064nm SMF. This data is fit to equation 4.4 and plotted with a perfect Gaussian beam of the same initial beam width for reference.

The output of the 1064nm fiber has a BPP of 1.1, which should couple nicely into a hollow core fiber or dielectric waveguide. The BPP is higher for the 1064nm SMF than the 1550nm SMF due to uncertainty in the characterization process. The coupling efficiency was 65% for the 1064nm SMF, which is a significant increase over the 1550nm SMF.

Once the system was fully aligned, the DPSS was characterized at the system output with the amplifiers turned off. This measurement was taken to ensure that the spatial quality was preserved until the Raman cell. Figure 4.6 indicates that the M^2 value at the system output is 1.1.

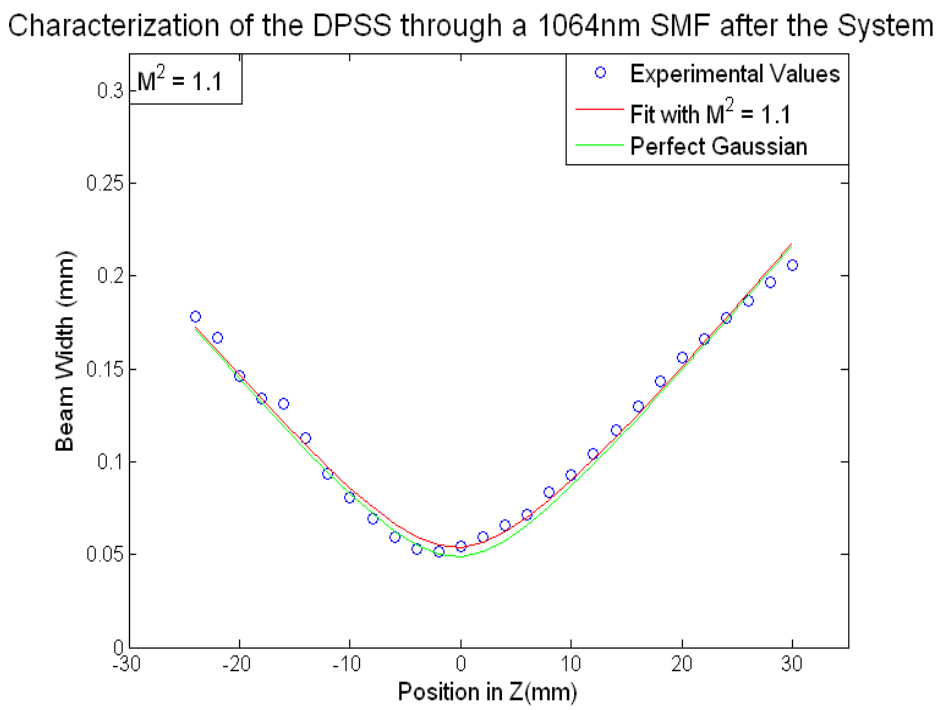

Figure 4.6: Beam size of the DPSS laser focused by a 200mm plano-convex lens after being spatially filtered by a 1064nm SMF and then passed through the amplification system. This data is fit to equation 4.4 and plotted with a perfect Gaussian beam of the same initial beam width for reference.

Characterization of the Amplified Pulses

Since the amplified pulses experience such dramatic temporal distortion, the spatial quality was checked after amplification. The amplified beam could not be characterized using the same technique that was used for the unamplified pulse due to the damage threshold of the CCD. Instead a razor blade was used to incrementally attenuate the beam while monitoring the transmitted energy, E_T. This data was then fit to the error function, which is arrived at when integrating over a Gaussian distribution shown in Equation 4.6. The position of the razorblade is notated by a in Equation 4.6. The beam width was first found without focusing the beam as shown in Figure 4.7.

$$E_T = \int_{-\infty}^{\infty} e^{-\frac{2y^2}{\omega^2}} dy \int_{-\infty}^{a} e^{-\frac{2x^2}{\omega^2}} dx \tag{4.6}$$

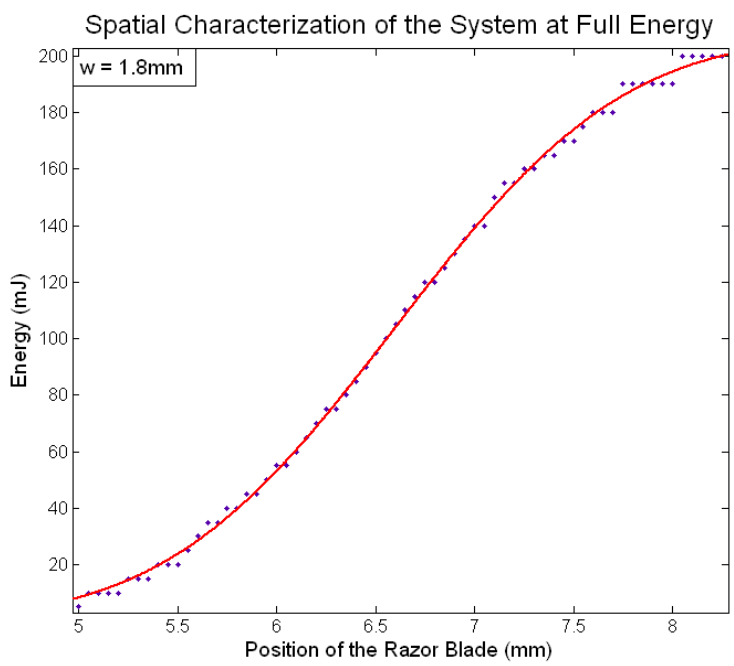

Figure 4.7: Transmitted energy versus position of the razor blade that clipped the unfocused beam.

Next the beam was sent through a focus where the razor blade method was repeated at three locations to find the M^2 value as shown in Figure 4.8. The beam width was checked at distances of one Rayleigh range near the beam waist. The beam waist was estimated from three data points and then compared to the calculated beam waist for a Gaussian beam. The M^2 value was found to be 2.0, which is a substantial increase from the unamplified beam. A commercial beam profiler would have proved extremely useful for characterizing the amplified output but was unfortunately not available.

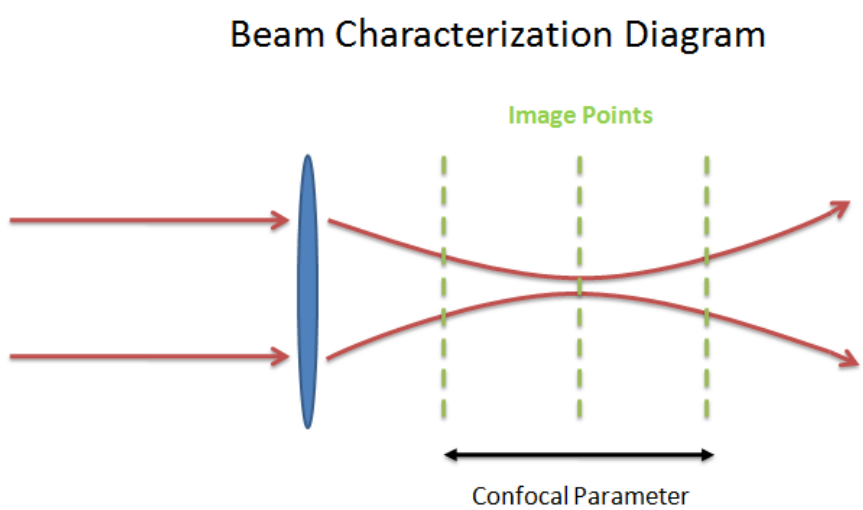

Figure 4.8: Illustrates how the three spot sizes of the focusing beam were measured with a CCD to determine the beam waist. The beam waist was then compared to the calculated beam waist of a perfect Gaussian to determine the M^2 value.

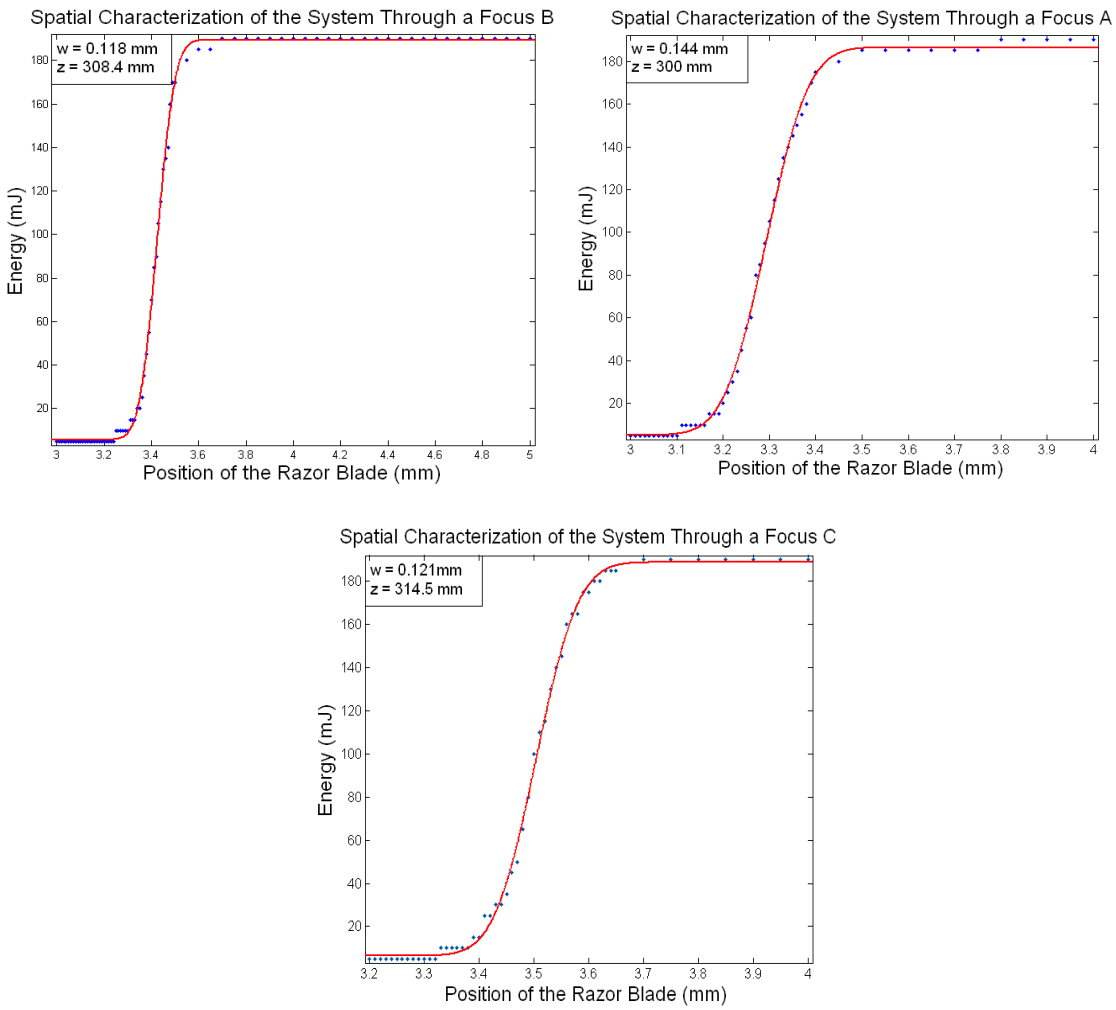

Figure 4.9-11: Transmitted energy versus position of a razor blade at three positions separated by the Rayleigh range (z_r = 8mm) near the beam waist. Each graph corresponds to a different location.

This severe decrease in the beam quality is attributed to saturation effects, which are more substantial at the center of the beam where the intensity is the highest. The overall effect is flattening of the spatial intensity distribution producing a super Gaussian spatial profile. The reduction in beam quality will increase the chances of optical damage when coupling into the fiber [22].

CHAPTER 5

FREQUENCY DOUBLING

A wave propagating through a dielectric material affects the temporal and spatial electron distribution of the atoms interacting with the electromagnetic field. This primarily affects only the valence electrons by forcing them from their unperturbed orbit. This results in many small electric dipoles, which on a macroscopic scale manifest the polarization. For small intensities the strength of the polarization is a linear function of the intensity of the incident wave. However, as the intensity increases the polarization will not necessarily follow the same oscillating form of the input wave [23].

$$P = \varepsilon_0 \chi^{(1)} E + \varepsilon_0 \chi^{(2)} EE + \varepsilon_0 \chi^{(3)} EEE + \ldots \qquad (5.1)$$

The polarization per unit volume, P, is given in terms of the permittivity of free space, ε_0 , the susceptibility, χ, and the magnitude of the electric field, E. The second term on the right hand side governs second harmonic generation and Optical Parametric Generation while the third term is responsible for optical Kerr effects and Raman effects among others. The first term describes the linear polarizing effect, which explains why some materials appear to be transparent. This section will only focus on the second term regarding second harmonic generation.

The wavelength generated by Nd:YAG or Nd:Vanadate is 1064nm. The desired wavelength for use in the Raman conversion studies is 532nm, which is the second

harmonic of 1064nm. Conversion to the second harmonic is possible by summing two waves to generate the desired third wave. The second harmonic generation process is the degenerate use of sum frequency generation. The three waves involved in this process are two incident 1064nm waves, which produce the 532nm output.

$$\frac{c}{1064nm} + \frac{c}{1064nm} = \frac{c}{532nm} \tag{5.2}$$

The polarization of the incident waves can vary depending on the type of second harmonic generation. There are three types that are categorized by the polarization of the waves in the birefringent material. Uniaxial crystals allow only one type of doubling while biaxial crystals allow more. In all cases, the two incident waves are referred to as the signal and the idler, and the frequency doubled wave is referred to as the pump. For SHG this notation seems counterintuitive, but it was developed for Optical Parametric Oscillation (OPO), which is essentially the reverse of frequency doubling. For efficient second harmonic generation (SHG), these three waves must be phase matched in the doubling crystal. Phase matching is illustrated in Figure 5.1.

The theory is rather complicated but experimental results are somewhat easy to obtain. Once the incident waves have the correct polarization and the crystal is of the appropriate length, it is just a matter of angle tuning the crystal until phase matching (or index matching) is obtained. Phase matching can be achieved through angle tuning because the index of refraction of the imaginary wave is a function of the angle between the wave's k vector and the orientation of the crystal. By adjusting the crystal's angle it is

possible to get all three waves to travel through the birefringent medium at the same speed. Once this is achieved, two 1064nm wave vectors in the crystal will add to equal one 532nm wave vector. In other words, angle tuning the crystal minimizes the phase mismatch, Δk. Phase matching occurs when Δk is equal to zero.

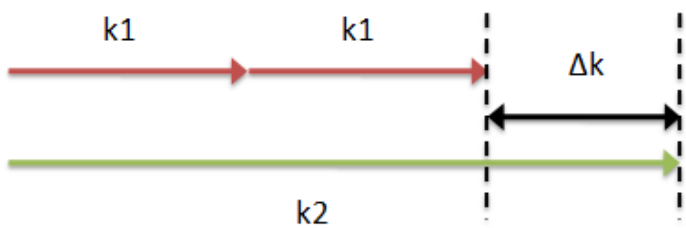

Figure 5.1: Illustration of phase matching required for the three waves involved in second harmonic generation.

To optimize the conversion efficiency the appropriate crystal length must be selected for the given beam intensity. Developing a model that accurately predicts the optimum crystal length begins with analyzing Maxwell's equations. The equation for a lossless, nonlinear dielectric medium leads to [23]:

$$\nabla^2 E + \mu_0 \varepsilon \frac{\partial^2 E}{\partial t^2} = -\mu_0 \frac{\partial^2 P_{NL}}{\partial t^2} \tag{5.3}$$

where P_{NL} is the nonlinear part of the polarization and is composed of the product of two incident E-fields.

$$P_{NL} = 2d_{ijk}E_jE_k \tag{5.4}$$

The nonlinear polarization is generated by the two incident E-fields. Again this process involves the mixing of three waves propagating in the z-direction which are described by the three equations below where the wave number is k, the angular frequency is ω and φ is their relative phase difference [24].

$$\begin{aligned} E_i(z,t) &= \frac{1}{2}[E_{1i}(z)e^{-i(k_1z-\omega_1t)+\varphi}] \\ E_k(z,t) &= \frac{1}{2}[E_{2k}(z)e^{-i(k_2z-\omega_2t)+\varphi}] \\ E_j(z,t) &= \frac{1}{2}[E_{3j}(z)e^{-i(k_3z-\omega_3t)+\varphi}] \end{aligned} \tag{5.5}$$

Substituting these traveling wave equations into Equation 5.4 produces three coupled differential equations. Making the additional substitution that $\omega = \omega_1 = \omega_2$ and $\omega_3 = 2\omega$, then only two coupled differential equations remain [23].

$$\begin{aligned} \frac{dE_\omega}{dz} &= i\omega\sqrt{\frac{\mu_0}{\varepsilon_\omega}}d_{ijk}E_{2\omega}E_\omega^*e^{-i\Delta kz} \\ \frac{dE_{2\omega}}{dz} &= -i\omega\sqrt{\frac{\mu_0}{\varepsilon_\omega}}d_{ijk}E_\omega^2e^{i\Delta kz} \end{aligned} \tag{5.6}$$

These equations can be solved for the conversion efficiency (after some simplification) given by Equation 5.7.

$$\eta_0 = C^2 L^2 I$$

$$\eta_m = 1 + \frac{\delta^2}{2\eta_0} - \sqrt{[1 + \frac{\delta^2}{2\eta_0}]^2 - 1}$$

$$\eta = \eta_m \mathrm{sn}^2[\sqrt{\frac{\eta_0}{\eta_m}}, \eta_m^2 \tag{5.7}$$

The conversion efficiency oscillates with a Jacobi ellipse, sn, where η is the conversion efficiency, δ is the dephasing term, and η_0 is called the drive. The drive is a function of the input intensity, I, length of the crystal, L, and the nonlinear coefficient of the crystal, C. The dephasing term is a function of the length of the crystal, beam divergence, and the angular sensitivity of the crystal. If used properly, Equation 5.7 will accurately predict the conversion efficiency of second harmonic generation. The initial results obtained to test the accuracy of these equations produced promising results as shown in Figure 5.2. The parameters used to predict the frequency conversion efficiency are the crystal's nonlinear coefficient, the crystal's angular sensitivity, the beam divergence, the beam intensity, and the length of the crystal. The model does not account for walk-off. The pump source used to take this data was the Monoblock laser from Scientific Materials and the birefringent material used was a scrap KTP crystal from

Quantel that had a damaged coating. The beam size was fortunately small enough to avoid the damaged region.

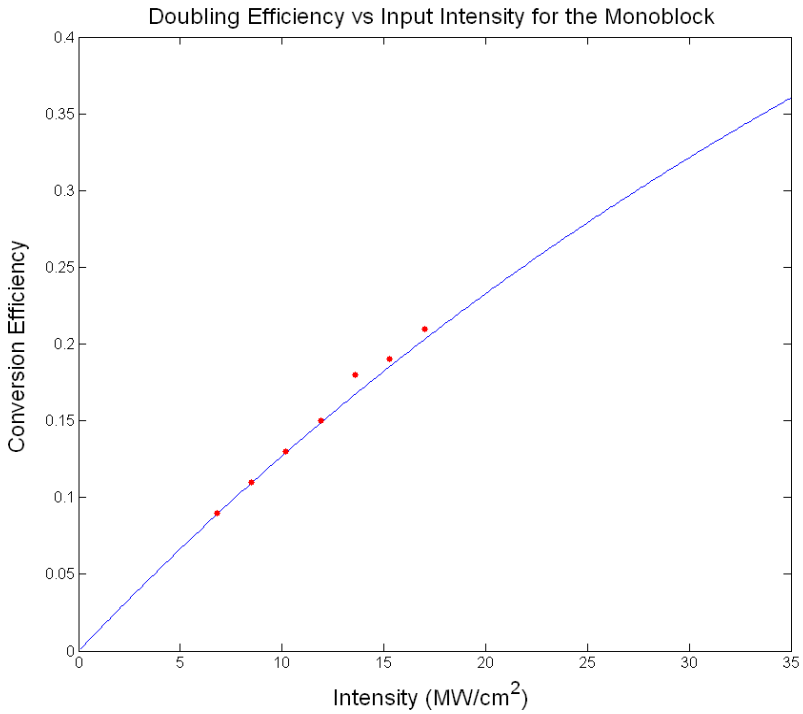

Figure 5.2: Frequency doubling efficiency versus input intensity for the Monoblock plotted with the predicted efficiency from Equation 5.7.

The frequency doubling efficiency of the full system behaved somewhat unusually as shown in Figure 5.3 (see Appendix D for modeling script). Rather than following the predicted efficiency as the Monoblock did, the conversion efficiency remained relatively constant as the amplifier energy increased. This interesting trend makes sense when the increasing spot size of the amplified pulse is considered. The spot size increased by a factor of four from the unamplified pulse and the pulse energy increased roughly linearly. The result of these two changing parameters could explain

why the conversion efficiency remained at a constant 30% with increasing pulse energy. To accurately model the efficiency it would be necessary to know the input intensity, which requires knowing the size of the beam as it changes with increasing energy. This measurement could be taken with a beam profile but one was not available. The predicted conversion efficiency is 32% at full energy where the beam width is known.

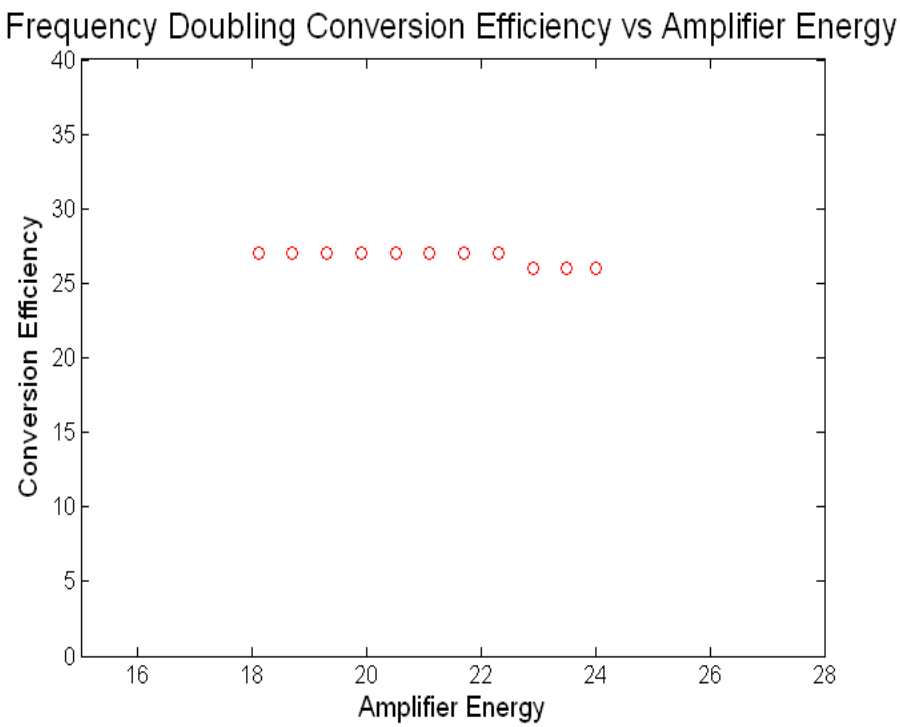

Figure 5.3: Frequency doubling efficiency of the laser system versus amplifier energy of the third amplifier. The constant conversion efficiency is due to the increasing beam width that changes as the amplifier energy is increased.

CHAPTER 6

WAVE GUIDES

Photonic Crystal Fiber

Traditional solid core optical fibers guide light through transparent glass via total internal reflection (TIR). TIR allows the light to reflect off the inner surface of the glass with theoretically no loss and is made possible because the glass has a higher index of refraction than the cladding. Recently a new type of hollow core fiber has emerged called-hollow core photonic crystal fiber (HC-PCF). This new type of fiber guides light in the same manner as photonic crystals, which use a photonic band gap. In HC-PCF's a two dimensional photonic band gap structure surrounds the hollow core and acts like a nearly perfect wave guide. These fibers can exhibit very low loss because the light can propagate through the air (or vacuum), making them potentially superior to traditional fibers currently used in telecommunications and other applications. They are also ideal for Raman scattering because they can guide light with high intensity over long interaction lengths in pressurized gas [25].

Coupling Into Photonic Crystal Fiber

The HC-PCF coupling efficiency was first tested with Coherent's 532nm Verdi laser. It was convenient to have access to the Verdi laser because it runs CW and has good spatial quality. The test fiber is designed for 532nm and has a small diameter of 5μm. The small size makes it rather difficult to couple light into but is ideal for Raman

scattering [26]. Fortunately, the mode field diameter of the fiber was provided by the manufacturer, Blaze Photonics, so it did not need to be calculated. It was specified to be 4µm for the 5µm fiber. To further aid in the coupling process the output of the fiber was sent into an optical microscope, which clearly indicated how the light was coupled into the fiber. A photograph of the fiber output is shown in Figure 6.1.

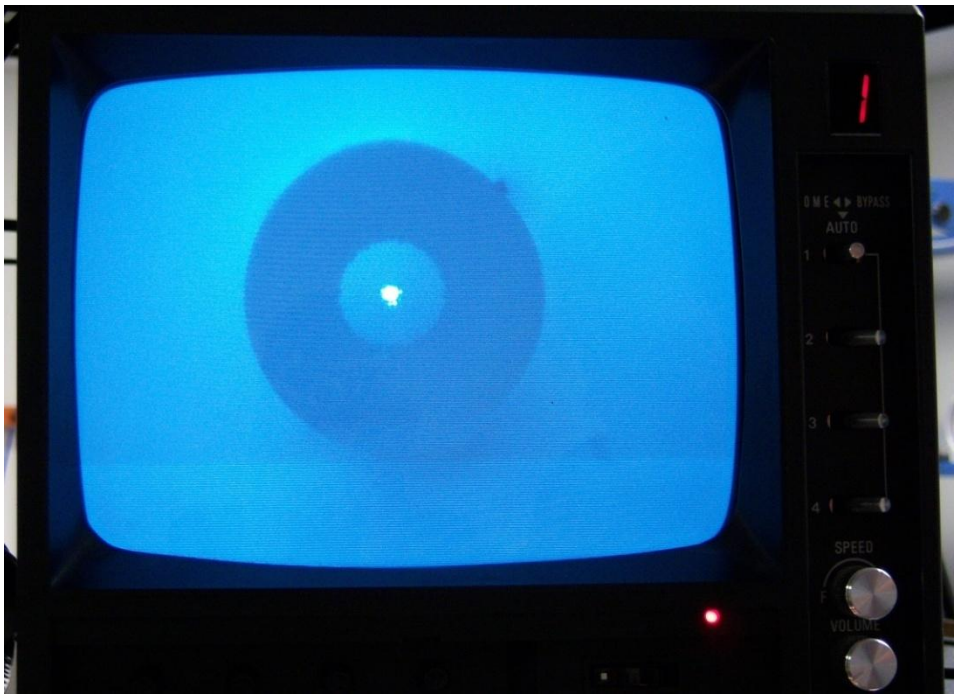

Figure 6.1: Photo of the output facet of the hollow core fiber imaged with an optical microscope used to aid the coupling process.

Initially, coupling light into the hollow core fiber was extremely problematic. The first issue encountered was the capillary effect that sucked up the solvent used to soften the cladding before cleaving. Placing dab of epoxy on the end of the fiber before dipping it in the solved resolved this issue. Another problem was with the amount of

light that was transmitted through the holey region of the fiber. The uncoupled transmitted light made it difficult to use the conventional method of coupling by optimizing the transmitted light on a detector. Fortunately, the optical microscope was a good substitute because it had high enough resolution to distinguish between light coupled into the holey region and light coupled into the desire center core. The mode matched coupling efficiency for the Verdi was 75%.

After confirming the theoretical coupling efficiency of the fiber with a CW source, the pulsed Monoblock laser mentioned in the previous section was used. Coupling with this laser proved to be very difficult because the maximum repetition rate of the laser is one hertz. Coupling with a beam of poor spatial quality produces an excess of energy incident on the holey region rather than the hollow core. This loss of energy not only reduces the coupling efficiency but also increases the likely hood of optical damage. The maximum coupling efficiency obtained was about 15% with the Monoblock.

It was initially thought that these fibers would be the best solution to achieve high energy Raman scattering. They work extremely well at low power, which was shown in the initial test setup. However, the holey region of the input facet has a low peak power threshold, which is susceptible to damage due to its small five micron inner core diameter. This makes coupling with high energy pulsed lasers difficult. During one test run the holey region of the output facet was fused together shortly after surpassing the Raman threshold. The pulse energy that damaged the fiber was only a few microjoules at a short six nanosecond pulse duration. The laser used for coupling in this experiment was

the Monoblock. The output of the Monoblock's beam is square with a uniform pulse distribution and is far from ideal for coupling. Although the beam was spatially filtered before coupling, it remained far from an ideal Gaussian.

In addition to the low damage threshold, the HC-PCF used in the initial tests was discontinued by Blaze Photonics and is not currently being manufactured by any other company. So even if the peak power damage threshold could be improved with a pump source of better spatial quality, there is not enough fiber left to reliably test its high energy Raman conversion capability. Interestingly, HC-PCF's proved to be quite resilient to the high average power experienced by the CW Verdi laser. The only power limitation found was that the cladding began to melt at about three watts. Choosing a different cladding, or providing cooling, should increase the average power limitation.

It was concluded that obtaining Raman scattering in the HC-PCF is possible but not at the desired energy due to the low damage threshold of the fiber. As a result of the optical damage and the unavailability of the HC-PCF, the decision was made to pursue capillaries as an alternative form of Raman cell. Capillaries are made of bulk glass rather than small tubes consequently increasing the potential damage threshold.

Capillaries

Though capillaries are superior to HC-PCF in regard to optical damage, they do present other concerns. The primary issue is their poor transmission, which decreases inversely with the radius of the capillary cubed. To make matters worse, the bending loss in capillaries increases inversely with the radius to the fourth power. Despite these

drawbacks, capillaries have already shown promising results with Raman scattering as mentioned in Chapter 1. For the short lengths that will be utilized in the Raman study, the ideal capillary core diameter was found to be about 100μm. At this diameter their theoretical transmission is 73% with minimal loss due to bending determined by Equations 6.1, 2 [27].

The capillary mode which propagates with a linear E-field has a spatial distribution of a zero order Bessel function. It is a superposition of transverse circular electric and transverse circular magnetic modes signified by EH_{11} shown in Figure 6.2. The transmission of the capillary modes can be calculated from the attenuation constant, α_s shown in Equation 6.1 where $u_{11} = 2.405$ is the first zero of the zero order Bessel function. The attenuation constant is in terms of the index of refraction of the capillary walls, υ, the wavelength of the guided light, λ, and the radius of the capillary, a [28]. The transmission, T, is shown in Equation 6.2.

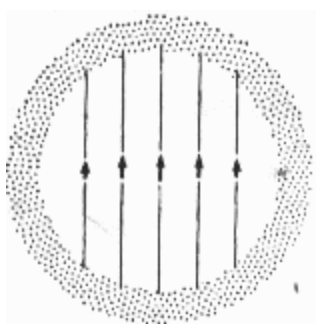

Figure 6.2: E-field of the hybrid EH_{11} mode, which has a first order Bessel function intensity distribution [27].

$$\alpha_s = \frac{1}{2}\left(\frac{u_{nm}}{2\pi}\right)^2\left(\frac{(v^2+1)}{\sqrt{v^2-1}}\right)\left(\frac{\lambda^2}{a^3}\right) \tag{6.1}$$

$$T = e^{-2\alpha_s l} \tag{6.2}$$

The three capillaries that were purchased have diameters of 50, 75 and 100 microns and are one foot long. These have the theoretical transmission of 8%, 47% and 73% respectively, assuming no bending loss. The poor transmission causes capillaries to glow when coupled with a visible laser as shown in Figure 6.3.

Figure 6.3: Photograph of a capillary coupled into with a Verdi laser. The capillary appears bright due to its high loss.

Capillaries are also susceptible to bending losses as previously mentioned. The total transmission coefficient, α, can be found by adding the bending transmission coefficient, α_b, as shown in Equation 6.3, to the straight waveguide transmission

coefficient, α_s. The bending loss is dependent on the radius of curvature, R and the angle between the plane of the radius of curvature and the orientation of the electric field, θ, among other previously mentioned variables.

$$\alpha_b = \frac{4}{3}\frac{a^3}{\lambda^2 R^2}\left(\frac{2\pi}{u_{nm}}\right)^2\left(\frac{\upsilon^2}{\sqrt{\upsilon^2-1}}\right) Re\{1 - \frac{n(n-2)}{u_{nm}{}^2} + \frac{3}{4}\delta(\mp 1)\frac{\upsilon^2-1}{\upsilon^2+1}\cos(2\theta)\} \qquad (6.3)$$

For a radius of curvature of 2m, the 50, 75 and 100 micron capillaries have theoretical transmission of 7%, 25% and 16% respectively. To reduce the risk of bending losses, a rigid V block was made to hold the capillaries straight inside the pressure chamber. It was decided to use the 100 micron capillary for the Raman study, which had an experimentally determined transmission of over 60%. This is agreeable to the theoretical value of 73% for a straight capillary [29].

Coupling into Capillaries

Unlike the fiber, there was no information available regarding the optical specifications on the capillaries purchased from Optical Fiber Center, Inc. According to the manufacturer, they were not generally intended to be used as optical waveguides. Therefore, the mode field diameter needed to be calculated in order to find the optimum coupling spot size. This required finding the spot size that maximized the overlap of the E-fields of the Gaussian beam and the Bessel function, which is the propagating mode in the capillary [27]. Like the HC-PCF, the capillaries were aligned with input beam by imaging the input and output facets shown in Figure 6.4.

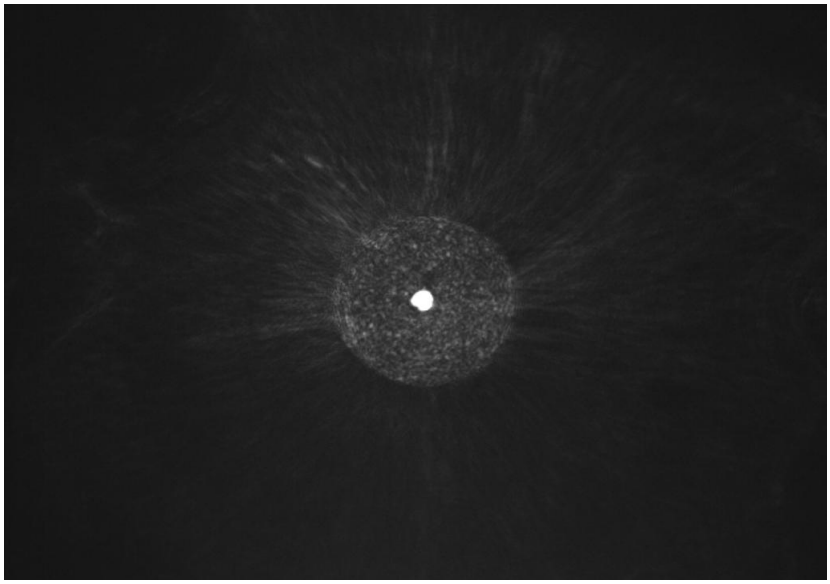

Figure 6.4: Output facet of a coupled 100 micron capillary imaged with a CCD. This imaging technique was used to aid the coupling process.

The spatial electric field distributions of the Gaussian beam and the capillary mode are given in Equations 6.4. The third equation is the inner product of the two fields that determines the overlap. The inner product was maximized for ω revealing the optimum Gaussian $1/e^2$ beam waist to be 64% of the capillary size as shown in Figure 6.5 (see Appendix E for modeling script). The theoretical result was experimentally tested and confirmed using a 100μm core capillary.

$$
\begin{aligned}
G &= \sqrt{\frac{2}{\pi}}\omega e^{\frac{-x^2}{\omega^2}} \\
B &= B_0 J_0(2.405\frac{r}{a}) \\
\langle G|B\rangle &= \int_0^a r dr \int_0^{2\pi} G^* B d\theta
\end{aligned}
\tag{6.4}
$$

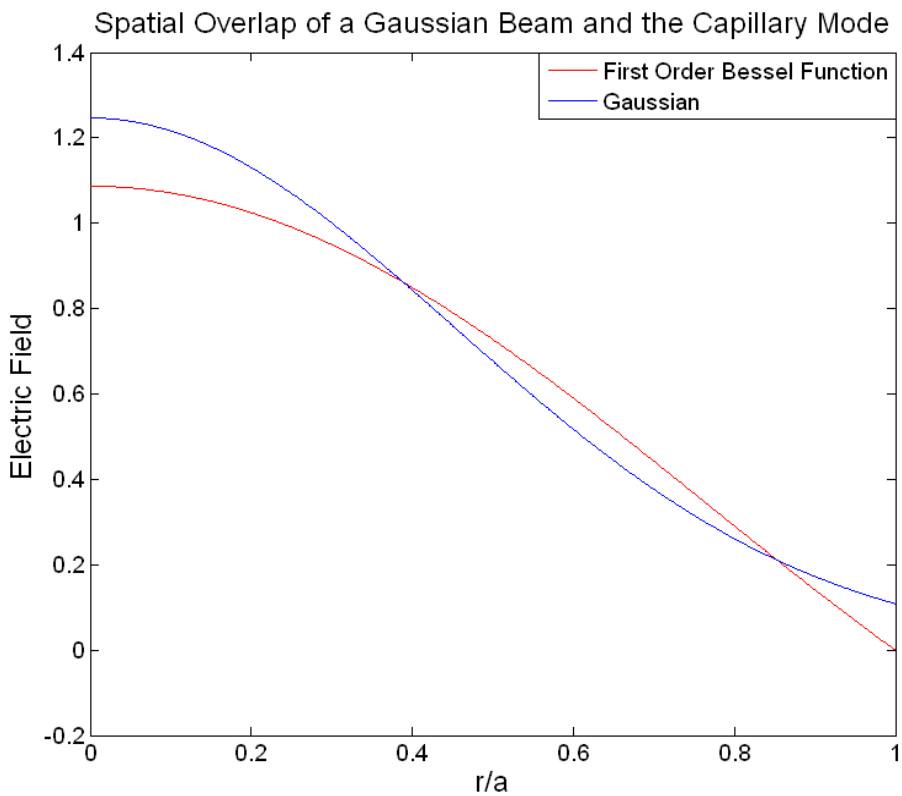

Figure 6.5: E-fields of the Gaussian beam with the beam width that optimized the spatial overlap with the Bessel function capillary mode.

It was also possible to calculate the theoretical maximum coupling efficiency. Once the optimum spot size was determined, a ratio of the overlap area to the total area under the Gaussian could be calculated. This ratio is the coupling efficiency assuming that the directions of the electric fields of both the Gaussian and capillary mode were the same shown in Figure 6.6. At the waist, the wave front of the Gaussian function is flat, which means the divergence is zero and that every component of the electric field is pointed in the z direction. This matches the capillary mode where all but a small portion of the E-field is oriented in the z direction, which validates the assumption [27]. The theoretical maximum coupling efficiency is 98%.

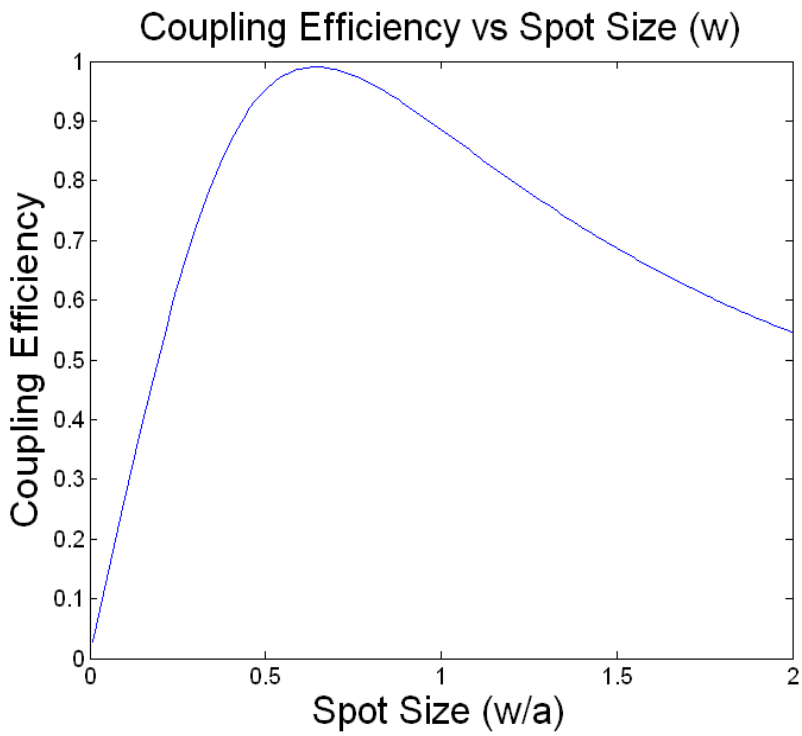

Figure 6.6: Capillary coupling efficiency verses beam size assuming that the input facet of the capillary is positioned at the beam waist.

CHAPTER 7

CONCLUSIONS

Laser System

The laser system successfully achieved a gain of 2.5×10^6, which produced the desired 200mJ pulses at 1064nm. The 1064nm was frequency doubled with 30% conversion efficiency, which could be improved by purchasing a doubling crystal of the desired length. So far the 30% efficiency has provided ample 532nm for the Raman study. Additionally, the temporal profile of these pulses can be predicted and controlled with the required precision to maintain a constant intensity throughout the duration of the pulse. In regard to energy and pulse shaping, the laser system is a success. The one area where the laser fell short was with the amplified spatial quality of $M^2 = 1.8$. The intent was to have a final beam quality of $M^2 < 1.1$. This M^2 parameter is the value used by manufacturers to specify the spatial quality of their single spatial mode lasers. The poor beam quality increases the risk of optical damage at the input facet of waveguides, which limits the maximum pump energy available for pumping the Raman cell.

There are several ways to improve the spatial quality of the amplified laser system. The optimum solution would be to find a more powerful seed source. The current input intensity into the AOM could be quadrupled without risk of optical damage making a more powerful seed source a practical solution. Having an initial pulse of higher energy would require less amplification to achieve the presently obtained energies. The decrease in amplification would reduce the amplification distortion, consequently

better conserving the spatial quality. Another potential solution would be to add another amplifier of preferably higher energy after the third amplifier in the current system. This would have essentially the same effect as increasing input pulse energy. The easiest solution to improving the beam quality would be to spatial filter the laser system's output. Unfortunately, this would substantially reduce the output energy and efficiency.

An additional change to the laser system being considered is seeding the DPSS with a distributed feedback laser operating at one longitudinal mode. Seeding the DPSS would provide two improvements to the laser system. The first is an improvement of the spatial quality, which might allow the spatial filter to be removed. Removing the spatial filter would increase the initial pulse energy by 40% and would not only increase the energy potential of the system but also reduce the amplified spatial distortion. Seeding the DPSS would also force the laser system to operate with only one longitudinal mode. Operating at only one longitudinal mode would not have a substantial impact on the laser system but could potentially increase the SRS gain.

Optical damage plagued this project from the beginning. At the start of the project, high energy equipment and optics were not available. The ticking sound of optical damage was, unfortunately, all too familiar while operating the laser system at high power. Consequently, over 30 optics were damaged during the construction and characterization process. The damaged optics include but are not limited to mirrors, lenses, PBSs, wave plates, PCFs, windows, capillaries, CCDs and even a high energy AOM. Some of the optical damage has been shown in Figures 7.1 and 7.2. Needless to

say, building the pump laser has been a learning experience, which will hopefully prevent optical damage in future endeavors [30].

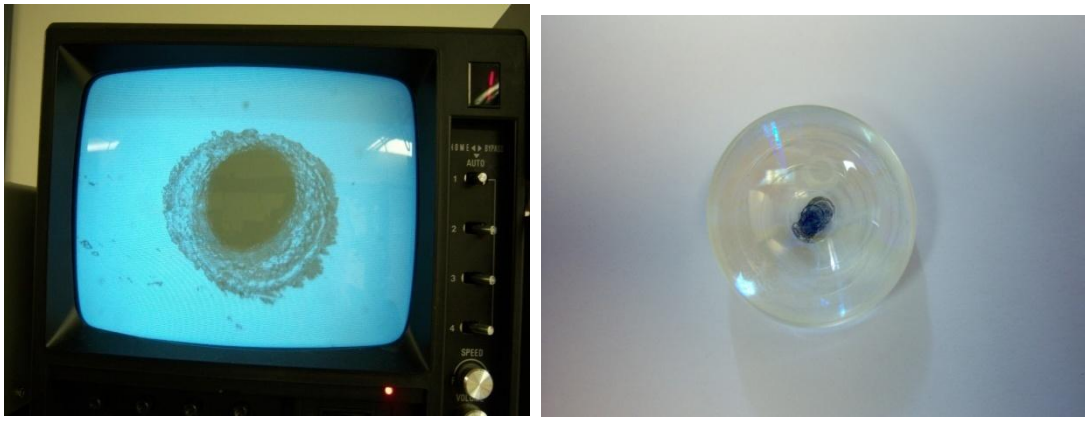

Figures 7.1-2: Optical damage in a sapphire window, which was part of the Raman cell, imaged with an optical microscope (left) and a damaged achromatic lens (right).

Recent Raman Results

Despite the poor spatial quality of the laser system, efficient SRS has recently been obtained with the laser pump source. The first time the pump laser was coupled into a capillary containing hydrogen gas, 1st, 2nd and 3rd vibrational Stokes and anti-Stokes shifts were generated. Immediately after obtaining these results, a quarter wave plate was placed in front of the Raman cell to circularly polarize the light. Circularly polarized photons carry angular momentum, which induces the 1st and 2nd rotational Stokes and anti-Stokes shifts as shown in Figure 7.3 [31]. SRS has also been seen in CO_2, which was an objective for this thesis. The CO_2 Stokes and anti-Stokes shifts are shown in Figure 7.4.

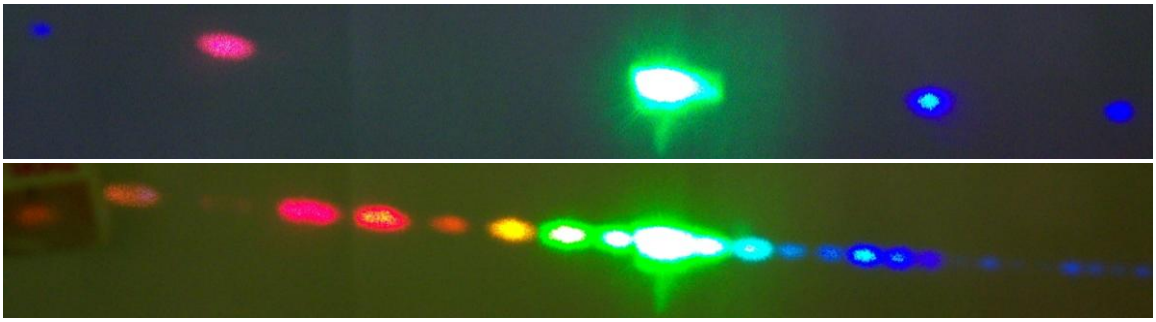

Figure 7.3: Photograph of vibrational (top) and rotational (bottom) Raman shifts in hydrogen courtesy of Dr. Barber, Dr. Reibel and Christoffer Renner.

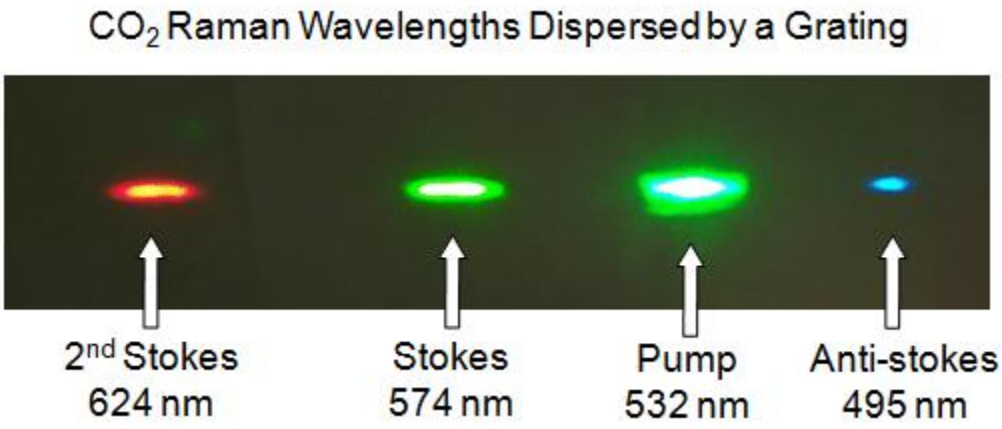

Figure 7.4: Vibrational Stokes and anti-Stokes shifts in hydrogen courtesy of Dr. Barber, Dr. Reibel and Christoffer Renner.

These initial results are very exciting and present the opportunity to study many interesting principles in physics. However, the primary objective of the project is to generate high conversion efficiency to the first order anti-Stokes as well as Stokes. The creation of the 2nd and 3rd order Stokes acts to suppresses the anti-Stokes making it difficult to achieve high conversion efficiency. A potential solution to this problem is to use HC-PCF rather than a capillary, whose transmission is strongly wavelength

dependant. In theory, a fiber could be used with high loss at the 2nd Stokes wavelength, which would allow unsuppressed amplification of the anti-Stokes [32].

This project is especially focused on anti-Stokes generation. It is hoped that efficient anti-Stokes is to be achieved through a four wave mixing process that requires the waves of different frequencies to be phase matched. The anomalous dispersion in capillaries, or waveguides, can compensate for the normal dispersion of the pressurized gas to make phase matching possible. The anti-Stokes should be sensitive to pressure tuning of the gas but this has yet to be seen experimentally. The Raman tests have only just begun due to the recent availability of the pump laser and there is still the anticipation of promising results [33-35].

REFERENCES CITED

[1] R. Reibel, DEPSCOR Proposal (2008)

[2] F. Benabid, G. Bouwmans, J. C. Knight and P.St. J. Russell, “Ultrahigh Energy Laser Wavelenght Conversion in a Gas-Filled Hollow Core Photonics Crystal Fiber by Pure Stimulated Rotational Raman Scattering in Molecular Hydrogen” PRL 93 (2004) 123903

[3] F. Benabid, G. Antonopoulos, J.C. Knight and P. St. J. Russel, “Stokes Amplification Regimes in Quasi-CW Pumped Hydrogen-Filled Hollow-Core Photonics Crystal Fiber” PRL 95 (2005) 213903

[4] B. Bobbs and C. Warner “Raman-Resonant Four-Wave Mixing and Energy Transfer” J. Opt. Soc. Am. 7 (1990) 234

[5] R. B. Miles and G. Laufer, “Coherent Anti-Stokes Raman Scattering in a Hollow Dielectric Waveguide” App. Phys. Lett. 30 (1977) 417

[6] R. K. Nubling, J. A. Harrington, “Launch Conditions and Mode Coupling in Hollow-Glass Waveguides” Opt. Eng. 37 (1998) 2454

[7] F. Benabid, J. C. Knight, G. Antonopoulos, P. St. J. Russell, “Stimulated Raman Scattering in Hydrogen-Filled Hollow-Core Photonics Crystal Fiber” Science 298 (2002) 399

[8] A. J. Berry and D. C. Hanna, “Stimulated Raman Oscillation in Capillary Waveguide Resonators” Opt. Com. 45 (1983) 35

[9] D. C. Hanna and M.T. T. Pacheco, “Higher-Stokes Order Raman Conversion to the Near Infrared: High Effeciency and Brightness via a Capillary Waveguide Amplifier” Opt. Com. 60 (1986) 107

[10] S. Zaitsu, H. Izaki and T. Imasaka, “Phase-Matched Raman –Resonant Four-Wave Mixing in a Dispersion-Compensated High-Finesse Optical Cavity” PRL 100 (2008) 073901

[11] W. E. Schmid “Pulse Stretching in a Q-Switched Nd:YAG Laser” J. Quantum Electronics, QE-16 (1980) 790

[12] M. J. Yarrow, J. W. Kim and W. A. Clarkson, “High Power Single-Frequency Continuous-Wave and Pulsed Nd:YVO_4 Master Oscillator Power Amplifier” OSA/ASSP MC6 (2006)

[13] Quantel USA, “Nd:YAG Laser System User Manual” CFR200/400, CFR800, Ultra CFR, DOC00054 Rev F

[14] N. P. Barnes and M. Walsh "Relaxation Oscillation Suppression in Nd:YAG Lasers Using Intra Resonator Harmonic Generation" Technical Report, NASA Langley Research Center

[15] Y. Tzuk, Y. Glick and M. M. Tilleman, "Compact Ultra-High Gain Mulit-Pass Nd:YAG Amplifier with a Low Passive Reflective Phase Conjugate Mirror" Opt. Com. 165 (1999) 237

[16] N. P. Barnes "Solid State Lasers from an Efficiency Perspective" Technical Report, NASA Langley Research Center

[17] N. S. Prasad, U. N Singh and F. Hovis, "High Energy, Single-Mode, All-Solid-State Nd:YAG Laser" Technical Report, NASA Langley Research Center (2006 or more recent)

[18] J. T. Verdeyen "Laser Electronics" Prentice Hall Series in Solid-State Physical Electronics 3rd Edition (1995)

[19] N. P. Barnes, T. J. Axenson, D. J. Reichle Jr. and B. M. Walsh "Diode-Pumped Laser Amplifier: Application to 0.946μm Nd:YAG" J. Phys. B: At. Mol. Opt. 36 (2003) 879

[20] D. Kincaid and W. Cheney, "Numerical Analysis: Mathematics of Scientific Computing" Ch. 8 Springer Wadsworth Group. Brooks/Cole 3rd Edition (2001)

[21] A. V. Smith and B. T. Do, "Bulk and Surface Laser Damage of Silica by Picosecond and Nanosecond Pulses at 1064nm" Applied Optics 47 (2008) 4812

[22] M.D Dawson, W.A. Schroeder, D.P. Norwood and A. L. Smirl, "Characterization of a High-Gain Picosecond Flash-Lamp-Pumped Nd:YAG Regenerative Amplifier" Opt. Lett. 13 (1998) 990

[23] W. Koechner, "Solid-State Laser Engineering" Springer Series in Opt. Sci. 6th Edition (2006)

[24] J. A. Armstrong, N. Bloembergen, J. Ducuing and P. S. Pershan, "Interactions Between Light Waves in a Nonlinear Dielectric" Phys. Rev. 127 (1962) 1981

[25] F. Couny, F. Benabid and P.S. Light " Large-Pitch Kagome-Structured Hollow-Core Photonics Crystal Fiber" Opt. Lett. 31 (2006) 3574

[26] R. K. James and J. A. Harrington, "Launch Conditions and Mode Coupling in Hollow-glass Waveguides" Opt. Eng. 37 (1998) 2454

[27] E. A. J. Marcatili and R. A. Schmeltzer, “Hollow Metallic and Dielectric Wave-guides for Long Distance Optical Transmission and Lasers” The Bell System Technical Journal. Jul (1964) 1783

[28] Y. Matsuura, T Abel and J. Harrington “Optical Properties of Small-Bore Hollow Glass Waveguides” App. Opt. 34 (1995) 6842

[29] C. G. Dufree III*, A. Rundquist, S. Backus, Z. Chang, C. Herne, H. C. Kapteyn and M. M. Murnane, “Guided-Wave Phase-Matching of Ultrashort-Pulse Light” J. Non. Opt. Phys. Mat. 8 (1999) 211

[30] O.Uteza, B. Bussiere, F. Canova, J. P. Chambaret, P. Delaporte, T. Itina, M. Sentis, “Laser-Induced Damage Threshold of Sapphire in Nanosecond, Picosecond and Femtosecond Regimes” Applied Surface Science 254 (2007) 799

[31] L. S. Meng, P. A. Roos and J. L. Carlsten, “Continuous-Wave Rotational Raman Laser in H_2” Opt. Lett. 27 (2002) 1226

[32] Schoulepnikoff and V. Mitev, “Numerical Method for the Modeling of High-Gain Single-Pass Cascade Stimulated Raman Scattering in Gases” J. Opt. Am. B 14 (1997) 62

[33] P. A. Roos, J. K. Brasseur and J. L. Carlsten, “Intensity-Dependant Refractive Index in a Nonresonant CW Raman Laser that is Due to Thermal Heating of the Raman-Active Gas” J. Opt. Soc. Am. B 17 (2000) 758

[34] J. K. Brasseur, R. F. Teehan, R. J. Knize, P. A. Roos and J. L. Carlsten, “Phase and Frequency Stabilization of a Pump Laser to a Raman Active Resonator” IEEE J. Quantum Electronics 37 (2001) 1075

[35] D. C. Hanna, D. J. Pointer and D. J. Pratt, “Stimulated Raman Scattering of Picosecond Light Pulses in Hydrogen, Deuterium and Methane” IEEE J. Quantem Electronics, QE-22 (1986) 332

APPENDICES

APPENDIX A

AMPLIFICATION MODEL

```
% Input Pulse Length (ns)
t = 1:200;

%Input Pulse Intensity (units of saturation intensity)
Io = 8*ones(200,1);

% Crystal parameters (L = length(cm), M = # of slices in z)
L = 10;
M = 100;

% Pulse parameters (N = length of slices in pulse)
N = 200;

% time
T = (1:N)';

% Ns = Initial population inversion (%):  a(k) is a vector containing %
% multiple Ns
for k = 1:length(a);
    Ns = a(k);

% Intensity (all time and space)
I = zeros(N,M);
I(:,1) = Io;

% Populations of ground, 1st excited and upper state states
X0 = zeros(N,M);
X0(1,:) = 1-Ns;
X1 = zeros(N,M);
% X1(1,:) = zero
X2 = zeros(N,M);
X2(1,:) = Ns;

% Gain factor (Scattering Cross Section times ion density): must
% specify for gain medium
G = 24.5;  % sigma = 18e-20cm^2, n = 1.36e20cm^-3

%%

for i = 1:1:N      % Time loop
    for j = 1:M     % Crystal loop

% Updates population levels for one slice of pulse passing
% through one slice of crystal
[T(i+1),X] = rk4step('Ndot_stage2',T(i),1,[X0(i,j) X1(i,j)
X2(i,j)],I(i,j));

% Update of intensity (an average population used in calculation
I(i,j+1) = I(i,j).*(1+G*((X2(i,j)+X(3))/2-(X1(i,j)+X(2))/2)*L/M);

% Relates outputs from rk4step to previously used notation
```

```
        X0(i,j) = X(1);
        X1(i,j) = X(2);
        X2(i,j) = X(3);

    end

    for j = M:-1:1     % Crystal loop, second pass

        [T(i+1),X] = rk4step('Ndot_stage2',T(i),1,[X0(i,j) X1(i,j)
X2(i,j)],I(i,j+1));

        X0(i+1,j) = X(1);
        X1(i+1,j) = X(2);
        X2(i+1,j) = X(3);

        I(i,j) = I(i,j+1).*(1+G*((X2(i,j)+X2(i+1,j))/2-
(X1(i,j)+X1(i+1,j))/2)*L/M);
    end

end

% Average gain in time over pulse
Gain(k)= mean(I(:,1)./(Io));

end
%%

% Plots final intensity output

figure(13)
plot(T(1:N),I(:,1),'g');
xlabel('Time (ns)')
ylabel('Intensity MW/cm^2')
title('Pulse Distortion')

 hold on

 % Plots gain vs input energy

% set the following parameters for plots
%  E = input energy of amplifier
%  b = experimentally found gain

 plot(T(1:N),10*Io,'r');

 figure(1)
 plot(E,190000*Gain,'r')
 xlabel('Amplifier Energy (J)','FontSize',14)
 ylabel('Gain','FontSize',14)
 title('Gain vs Amplifier Energy','FontSize',18)
```

```
 hold on

plot(E,b,'o');

hold off


% new file 'ndot_stage2, contains rate equations used to track ion
% populations

function Ndot = Ndot(t,n,Inputs)

tau2 = 255e3;
tau1 = 30;
tau21 = 1/.17*tau2;
tau20 = 1/(1/tau2-1/tau21);
R2 = 0;    %Inputs(:,1);
Iin = Inputs;%Inputs(floor(t+1),1);
Isat = 4.4e3;
R1 = 0;
N0 = n(1);
N1 = n(2);
N2 = n(3);
N2dot = R2 - N2/tau2 - Iin/tau2*(N2-N1); %- Ispon/tau2*(N2-N1);
N1dot = R1 + N2/tau21 + Iin/tau2*(N2-N1) - N1/tau1;
N0dot = N1/tau1 - R2 - R1 + N2/tau20;
Ndot = [N0dot N1dot N2dot];
```

APPENDIX B

GAUSSIAN INTENSITY DISTRIBUTION FIT

```
NLoops = 10;   % Number of loops to cycle through

% # of Camera pixals (x,y axis)
NPix_x = 512;
NPix_y = 384;

% Camera pixal size (x,y axis)
dx = 0.00465;
dy = 0.00465;

% Establishes size of CCD
xv = (1:1:NPix_x)*dx;
yv = (1:1:NPix_y)*dy;

[x,y] = meshgrid(xv,yv);

% Initialize camera (requires Matlab image acquisition toolbox)
[vid,vid_src]=CreateVidSrc(10);

for i = 1:NLoops
% Grab the data from camera, z = frame
z = getsnapshot(vid);

% Shows beam
figure(30)
imshow(z);
z = double(z);
figure(30)

% Summing Over Elements
z_x = sum(z);
z_y = sum(z');

% Calculating Center of Mass
cmy = sum(yv.*z_y)/sum(z_y);
iy = round(cmy/0.00465);

cmx = sum(xv.*z_x)/sum(z_x);
ix = round(cmx/0.00465);

% Extracts cross sections profiles of beam at center of mass
a = z(iy,:);
b = z(:,ix)';

%%

% Initial guesses for amplitude (pixel int), center location (mm), and
% spot size (mm)
if i == 1
    param1 = [1.5,1,1];
   param2 = [1.5,1,1];
else
```

```
    param1 = [Aox(i-1),xox(i-1),sigmax(i-1)];
   param2 = [Aoy(i-1),xoy(i-1),sigmay(i-1)];

end

% fits Gaussian to data on x and y axis
options =  optimset('TolX',1e-
12,'MaxIter',100000,'MaxFunEvals',100000);
g = fminsearch(@DiffGuassSpatial_3DCM,param1,options,0,xv,a);

Aox(i) = g(1);
xox(i) = g(2);
sigmax(i) = g(3);

options =  optimset('TolX',1e-
12,'MaxIter',100000,'MaxFunEvals',100000);
h = fminsearch(@DiffGuassSpatial_3DCM2,param2,options,0,yv,b);

Aoy(i) = h(1);
xoy(i) = h(2);
sigmay(i) = h(3);

% Shows fit

     figure(10)
     plot(xv,a);
     DataGuassx = Aox(i)*exp(-2*(xv-xox(i)).^2/sigmax(i).^2);
     hold
     plot(xv,DataGuassx,'r:')
     hold off
     figure(20)
     plot(yv,b);
     DataGuassy = Aoy(i)*exp(-2*(yv-xoy(i)).^2/sigmay(i).^2);
     hold
     plot(yv,DataGuassy,'r:')
     hold off

end

% Close the camera
CloseVidSrc(vid);



% New file:  diffgaussspatial_3dcm2


function [r] = DiffGuass(param,Bkgd,xv,b);
%   Finds the difference of a gaussian and the actual data

Ao = param(1);
```

```
xo = param(2);
sigmax = param(3);

% Gaussian intensity distribution (I=E*E)
yt = Ao*exp(-2*(xv-xo).^2/sigmax.^2)-Bkgd;
r = norm(b-yt);
```

APPENDIX C

BPP CHARACTERIZATION

```
% x1 = location in z where z=0 corresponds to beam waist (mm)
xvals = x1;

% measured spot sizes corresponding to x1 (mm)
yvals = y1;

beta0 = [.06 1 0]; % Initial guesses for (w0 M2 Z0)

% Runs fitting program to Guassian beam equation in beamwaistfitM2, be
% sure to set wavelength in beamswaistfitM2
[beta,r,J] = fitnonlin(xvals,yvals,'beamwaistfitM2',beta0);

%yfit = beamwaistfit([.054 -1],xfit);
yfit = beamwaistfitM2([beta(1) beta(2) beta(3)],xvals);

% Plot of beam if it were perfect Gaussian (for reference)
ym1 = beamwaistfitM2([beta(1)/beta(2) 1 beta(3)],xvals);

figure(1)
%plot(xvals,yvals,'o',xvals,yfit,'r')
plot(xvals,yvals,'o',xvals,yfit,'r',xvals,ym1,'g')

hold on
xlabel('Position in Z(mm)','FontSize',14)
ylabel('Sigma (mm)','FontSize',14)
title('Characterization of the DPSS','FontSize',18)

reduced_chi2 = sum(r.^2)/(1e-3)^2/(length(xvals)-3);



% Separate file:  beamwaistfitM2

function y = beamwaistfitM2(beta,z)

w0 = beta(1);
z0 = beta(3);
M2 = beta(2);

% Rayleigh range, set wavelength (mm)
zr = pi*w0^2/(M2*(1064e-6));

% beam waist in the direction of propagation(z)
y = sqrt(w0^2*(1+((z-z0)./zr).^2));



% Separate file:  fitnonlin

function [beta,r,J] = fitnonlin(X,y,model,beta0)
```

```
%NLINFIT Nonlinear least-squares data fitting by the Gauss-Newton
method.
%   NLINFIT(X,Y,FUN,BETA0) estimates the coefficients of a nonlinear
%   function using least squares.  Y is a vector of response (dependent
%   variable) values.  Typically, X is a design matrix of predictor
%   (independent variable) values, with one row for each value in Y.
%   However, X may be any array that FUN is prepared to accept.  FUN is
%   a function that accepts two arguments, a coefficient vector and the
%   array X, and returns a vector of fitted Y values.  BETA0 is a
vector
%   containing initial values for the coefficients.
%
%   [BETA,R,J] = NLINFIT(X,Y,FUN,BETA0) returns the fitted coefficients
%   BETA, the residuals R, and the Jacobian J.  You can use these
outputs
%   with NLPREDCI to produce error estimates on predictions, and with
%   NLPARCI to produce error estimates on the estimated coefficients.
%
%   Examples
%   --------
%   FUN can be specified using @:
%      nlintool(x, y, @myfun, b0)
%   where MYFUN is a MATLAB function such as:
%      function yhat = myfun(beta, x)
%      b1 = beta(1);
%      b2 = beta(2);
%      yhat = 1 ./ (1 + exp(b1 + b2*x));
%
%   FUN can also be an inline object:
%      fun = inline('1 ./ (1 + exp(b(1) + b(2)*x))', 'b', 'x')
%      nlintool(x, y, fun, b0)
%
%   See also NLPARCI, NLPREDCI, NLINTOOL.

%   Copyright 1993-2002 The MathWorks, Inc.
% $Revision: 2.22 $  $Date: 2002/01/17 21:31:27 $

if (nargin<4), error('NLINFIT requires four arguments.'); end

if min(size(y)) ~= 1
   error('Requires a vector second input argument.');
end
y = y(:);

if size(X,1) == 1 % turn a row vector into a column vector.
   X = X(:);
end

wasnan = (isnan(y) | any(isnan(X),2));
if (any(wasnan))
   y(wasnan) = [];
   X(wasnan,:) = [];
end
```

```
n = length(y);

p = length(beta0);
beta0 = beta0(:);

if any(size(feval(model,beta0,X)) ~= size(y))
   error('FUN should return a column vector of the same length as Y.');
end

J = zeros(n,p);
beta = beta0;
betanew = beta + 1;
maxiter = 5000;
iter = 0;
betatol = 1.0E-6;
rtol = 1.0E-6;
sse = 1;
sseold = sse;
seps = sqrt(eps);
zbeta = zeros(size(beta));
s10 = sqrt(10);
eyep = eye(p);
zerosp = zeros(p,1);

while (norm((betanew-beta)./(beta+seps)) > betatol | abs(sseold-
sse)/(sse+seps) > rtol) & iter < maxiter
   if iter > 0,
      beta = betanew;
   end

   iter = iter + 1;
   yfit = feval(model,beta,X);
   r = y - yfit;
   sseold = r'*r;

   for k = 1:p,
      delta = zbeta;
      if (beta(k) == 0)
         nb = sqrt(norm(beta));
         delta(k) = seps * (nb + (nb==0));
      else
         delta(k) = seps*beta(k);
      end
      yplus = feval(model,beta+delta,X);
      J(:,k) = (yplus - yfit)/delta(k);
   end

   Jplus = [J;(1.0E-2)*eyep];
   rplus = [r;zerosp];

   % Levenberg-Marquardt type adjustment
   % Gauss-Newton step -> J\r
```

```
   % LM step -> inv(J'*J+constant*eye(p))*J'*r
   step = Jplus\rplus;

   betanew = beta + step;
   yfitnew = feval(model,betanew,X);
   rnew = y - yfitnew;
   sse = rnew'*rnew;
   iter1 = 0;
   while sse > sseold & iter1 < 12
      step = step/s10;
      betanew = beta + step;
      yfitnew = feval(model,betanew,X);
      rnew = y - yfitnew;
      sse = rnew'*rnew;
      iter1 = iter1 + 1;
   end
end
if iter == maxiter
   disp('NLINFIT did NOT converge. Returning results from last
iteration.');
end
```

APPENDIX D

FREQUENCY DOUBLING MODEL

```
%Second Harmonic Efficiency Calculator

% C: Nonlinear coefficient of the crystal
C = sqrt(1/21);

% S: Angle sensitivity of the crystal
S = 0.32;

% D: Beam divergence (mrads)
D = 10;

% I: Beam intensity (MW/cm^2)
I = 1:25;

% L: Crystal length (cm)
L = 1;

drive = (C.^2).*(L.^2).*I;
dephasing =.25*L.*D.*S;


% Emax: Maximum possible efficiency
Emax = 1+((dephasing.^2)./(2*drive))-
sqrt(((1+(dephasing.^2)./(2*drive)).^2)-1);


% E: Actual efficiency for a given crystal length
E = Emax.*(ellipj(sqrt(drive./Emax),(Emax.^2))).^2;

%%
%Plot of Efficiency vs Crystal Length
figure
plot(I,E)
hold on
%plot(shgData(:,1),shgData(:,2),'x');
%figure; plot(shgData(:,1),shgData(:,2),'x');
%legend('SHG','SHG')
xlabel('Intensity (MW/cm^2)','FontSize',20)
ylabel('Conversion Efficiency','FontSize',20)
```

APPENDIX E

GAUSSIAN AND BESSEL FUNCTION E-FIELD OVERLAP

```
% Maximize the overlap of a Gaussian and a Bessel function

% # of iterations
N = 200;
for i = 1:1:N;

dr = 0.001;
r = 0:dr:1;
G = zeros(N,length(r));


% w = Spot size
dw = .01;
w(i) = dw*i;

% Normalization of Bessel Function (from zero to one)
Bo = sqrt(1/(2*pi*dr*sum(r.*(Besselj(0,2.405*r).^2))));

% Normalization of Gaussian Function (from zero to infinite)
    % analytical normalization
Go(i) = sqrt(2/pi)/(w(i));

    % numerical normalization
% Go(i) = sqrt(1/(dr*sum(exp(-2*(r).^2/w(i).^2))));

%Zeroeth Order Bessel Function (E field inside capillary)
B = Bo*Besselj(0,2.405*r);

% Gaussian Function (E field of incident beam)
G(i,:) = Go(i)*exp(-(r).^2/(w(i).^2));

% Calculating Overlap Area (via inner product)
A(i) = 2*pi*dr*sum(r.*B.*G(i,:));
end

% Maximizing Overlap Area For Beam Waist(w)
% s = maximum theoretical coupling efficiency
% I = w value that maximizes A
% A = overlap area
figure(6)
plot(w,A)
[s,I] = max(A);
w_optimum = w(I);%I*dw;
xlabel('Spot Size (w/a)')
ylabel('Coupling Efficiency')
title('Coupling Efficiency vs Spot Size (w)')

% Plot
figure(10)
plot(r,B,'r');
hold on
plot(r,G,'b');
```

```
% Normalization Check (they should equal to or less than one)
for n = 1:1:N;
G_check(n) = sum(2*pi*r.*(G(n,:).^2))*dr;
end
B_check = dr*sum(2*pi*r.*(B.^2));

xlabel('Trial Number')
ylabel('Electric Field')
title('Overlap of Bessel with test Gaussian functions')



figure (77)
plot(G_check);
xlabel('Trial Number')
ylabel('Normalization of Gaussian in the Capillary')
title('Normalization Check')


% Cross Sectional Plot of Best fit
figure (88)
plot(r,B,'r',r,G(I,:),'b');
xlabel('r/a')
ylabel('Electric Field')
title('Cross Sectional Overlap of Electric Fields in 2D')
```